

AN ABSTRACT OF THE THESIS OF

Gerrit T. Gardner for the degree of Master of Science in Geology presented on August 22, 2017.

Title: Groundwater Flow Modeling at Santa Susana Field Laboratory, California.

Abstract approved:

Roy Haggerty

Understanding groundwater flow in faulted and fractured rock is an important frontier in the field of environmental remediation and in the management of water resources. One example of a site where this is particularly evident is the Santa Susana Field Laboratory (SSFL) in Ventura County, CA where environmental remediation activities have been underway for decades. A major challenge at the SSFL is accounting for the influences of various geological structures at the local scale. To support this effort, this study employs numerical modeling as a method to understand groundwater flow at one area of the SSFL where a well transect through a fault zone exhibits anomalous water levels. For this study, a two-dimensional cross-section continuum model was constructed along the well transect to simulate flow at the area. Several simulations were run to investigate several combinations of fault hydraulic character and fracture network connectivity. Water levels measured at wells in the transect were used as criteria for calibrating the simulation scenarios. Results suggests that at least the upper part of the fault zone is a barrier to groundwater flow. However,

head matching alone was not sufficient to be able to say with certainty if the low-conductivity condition extends deeper along the fault zone or if there is significant connectivity in the fracture network to overprint rock matrix anisotropy. Simulation results were also viewed in light of which ones would be most likely to produce the shape of the existing contamination plume. These observations most strongly support a system with strong bedding parallel anisotropy. Some evidence seemed to suggest that the fault.

©Copyright by Gerrit T. Gardner
August 22, 2017
All Rights Reserved

Groundwater Flow Modeling at Santa Susana Field Laboratory, California

by
Gerrit T. Gardner

A THESIS

submitted to

Oregon State University

in partial fulfillment of
the requirements for the
degree of

Master of Science

Presented August 22, 2017
Commencement June 2018

Master of Science thesis of Gerrit T. Gardner presented on August 22, 2017

APPROVED:

Major Professor, representing Geology

Director of the College of Earth, Ocean, and Atmospheric Sciences

Dean of the Graduate School

I understand that my thesis will become part of the permanent collection of Oregon State University libraries. My signature below authorizes release of my thesis to any reader upon request.

Gerrit T. Gardner, Author

ACKNOWLEDGEMENTS

I express my appreciation to Dr. Roy Haggerty for taking a risk on a timid prospective grad student and for guiding me through this process. I also express gratitude to Dr. Aaron Wolf who first put me in touch with Dr. Haggerty and without whom I would not have come to OSU. A very special thanks to Paul Hsieh of the USGS for serving on my committee as a non-faculty volunteer, for devoting his time and considerable talents to mentoring me, and for going out of his way to be present at my thesis defense. I would also like to acknowledge John and Shirley Byrne whose donation to the Hollis Dole Foundation provided means for me to take a modeling course in Berlin. I would like to thank NASA for allowing access to their documents and use of their data. Another special thank you goes to Pete Lawson and others at CH2M Hill for helping to provide the platform for this thesis, and for contributing valuable advice all along the way. Most of all, I thank my wife, Haley, whose support and encouragement never wavered despite my own uncertainties.

TABLE OF CONTENTS

	<u>Page</u>
Chapter 1: Introduction.....	1
1.1 Scope and Purpose.....	1
1.2 Intellectual Context.....	2
Chapter 2: SSFL Description.....	4
2.1 SSFL Overview.....	4
2.1.1 Geography.....	4
2.1.2 Operations and Environmental Impact.....	5
2.1.3 Remediation Efforts.....	6
2.2 Geology and Hydrogeology.....	8
2.2.1 Chatsworth Formation.....	8
2.2.2 Structural Geology.....	12
2.2.3 Hydrogeology.....	12
2.3 B204 Area and the North Fault Zone.....	15
2.3.1 Local Stratigraphy and Structure.....	18
2.3.2 Groundwater Elevations.....	18
Chapter 3: Modeling Methods.....	23
3.1 Overview of Objectives and Methods.....	23
3.2 Conceptual Model.....	24
3.2.1 Recharge and Discharge Conceptualization.....	25
3.2.2 NFZ Conceptualization.....	25
3.2.3 Hydraulic Conceptualization.....	26
3.3 Mathematical Model.....	27
3.3.1 Study Approach.....	27
3.3.2 Governing Equations.....	29
3.3.3 Finite Element Method.....	31
3.4 Simulation Model Design and Calibration.....	32
3.4.1 Model Construction.....	32
3.4.2 Boundary Conditions.....	35

TABLE OF CONTENTS (CONTINUED)

	<u>Page</u>
3.4.3 Parameters of Interest.....	36
3.4.4 Simulation Scenarios.....	37
Chapter 4: Results and Discussion.....	40
4.1 Anisotropic Simulations.....	40
4.1.1 Scenarios without NFZ.....	40
4.1.2 Uniform Fault Barrier Scenario.....	43
4.1.3 Partial Fault Barrier Scenario.....	46
4.2 Isotropic Simulations.....	49
4.2.1 Scenarios without NFZ.....	49
4.2.2 Uniform Fault Barrier Scenario.....	52
4.2.3 Partial Fault Barrier Scenario.....	55
4.3 Discussion.....	58
4.3.1 Simulation Comparisons.....	58
4.3.2 Comparison with Other Observations.....	60
4.3.3 Implications.....	61
Chapter 5: Conclusions and Recommendations.....	63
5.1 Conclusions.....	63
5.2 Recommendations.....	64
References.....	65
Appendices.....	67

LIST OF FIGURES

<u>Figure</u>	<u>Page</u>
2.1 SSFL Location Map.....	4
2.2 SSFL Regional Setting.....	5
2.3 2009 Mountain Scale SCM.....	7
2.4 Regional Geologic Map.....	9
2.5 Geologic Map of Chatsworth Formation.....	10
2.6 Chatsworth Formation Stratigraphic Column.....	11
2.7 Chatsworth Formation Geologic Cross Section.....	13
2.8 SSFL Fault Orientations.....	14
2.9 SSFL Seep Locations.....	16
2.10 B204 Area Map.....	17
2.11 B204 Area Cross Section.....	20
2.12 B204 Area Chatsworth Formation Groundwater Elevation Map.....	21
2.13 B204 Area Hydrogeologic Cross Section.....	22
3.1 Modeling Process Flow Chart.....	24
3.2 Fracture Flow Study Approaches.....	28
3.3 Finite Element Mesh Example.....	32
3.4 Model Cross Section Line.....	33
3.5 Simulation Model Construction Diagram.....	34
3.6 Simulation Scenarios.....	39
4.1 Results of Anisotropic Homogenous Simulation.....	41
4.2 Results of Anisotropic Simulation with Fine-grained Units.....	42
4.3 Initial Results of Anisotropic Uniform Barrier Simulation.....	44
4.4 Calibrated Results of Anisotropic Uniform Barrier Simulation.....	45
4.5 Initial Results of Anisotropic Partial Barrier Simulation.....	47
4.6 Calibrated Results of Anisotropic Partial Barrier Simulation.....	48
4.7 Results of Isotropic Homogeneous Simulation.....	50
4.8 Results of Isotropic Simulation with Fine-grained Units.....	51
4.9 Initial Results of Isotropic Uniform Barrier Simulation.....	53
4.10 Calibrated Results of Isotropic Uniform Barrier Simulation.....	54

LIST OF FIGURES (CONTINUED)

<u>Figure</u>	<u>Page</u>
4.11 Initial Results of Isotropic Partial Barrier Simulation.....	56
4.12 Calibrated Results of Isotropic Partial Barrier Simulation.....	57

LIST OF TABLES

<u>Table</u>	<u>Page</u>
3.1 van Genuchten Parameters.....	31
4.1 Calibrated Conductivity Values for Anisotropic Uniform Barrier Simulation.....	43
4.2 Calibrated Conductivity Values for Anisotropic Partial Barrier Simulation.....	46
4.3 Calibrated Conductivity Values for Isotropic Uniform Barrier Simulation.....	52
4.4 Calibrated Conductivity Values for Isotropic Partial Barrier Simulation.....	55
4.5 Summary Matrix of Simulation Results.....	61

LIST OF APPENDICES

<u>Appendix</u>	<u>Page</u>
Appendix A: Mesh Development.....	66
Appendix B: Solution Validation.....	68
Appendix C: Water Level Data.....	71

DEFINITIONS OF ABBREVIATIONS

AIG	area of impacted groundwater
B204	Building 204
COC	contaminant of concern
DFN	discrete fracture network
DNAPL	dense non-aqueous phase liquid
DTSC	Department of Toxic Substances Control
ELV	expendable launch vehicle
EPM	equivalent porous medium
FDM	finite difference method
FEM	finite element method
NFZ	North Fault Zone
SCM	site conceptual model
SPA	storable propellant area
SSFL	Santa Susana Field Laboratory
TCE	trichloroethylene

Chapter 1: Introduction

1.1 Scope and Purpose

Groundwater remediation projects are important for maintaining clean water supply, especially in arid regions where surface water sources are sparse and already overtaxed. One of the larger scale remediation efforts in the U.S. is taking place at the Santa Susana Field Laboratory (SSFL) in Ventura County, California where groundwater remediation efforts have been under way for over three decades (Cilona et al., 2016). Despite the considerable time and vast resources spent, a working remediation strategy has yet to be implemented. One reason for this is that the size and complexity of the groundwater system make accurate characterization of groundwater flow a particularly difficult task. As a rule, accurate characterization of contaminant transport requires an accurate characterization of groundwater flow. Therefore, filling gaps in understanding of groundwater flow at contaminated sites should be a high priority endeavor.

At this stage, most of the unknowns at the SSFL relate to the hydraulic characteristics of local features such as fault zones. For example, whereas recharge, discharge, and flow directions are reasonably well understood at the regional and local scales, the effect of local faults on groundwater flow paths at some critical remediation areas is not as well constrained. Consequently, the regional and local scale numerical models that are used to make remediation decisions do not do not reflect these influences. One such area is the B204 area of the SSFL where anomalous water levels near a fault zone have been problematic for remedial design developers. The objective of this thesis is to develop a small scale numerical flow model to assist in understanding groundwater flow at the B204 area. This study serves as a supplement to work being done for the most recent B204 characterization report. The hope is that this thesis will be

valuable in refining the conceptual model for contaminant transport at the B204 area and thereby assist in making recommendations for remedial action.

1.2 Intellectual Context

The characterization of the SSFL groundwater system has produced one of the world's most extensive data sets describing a fractured sedimentary rock aquifer (MWH, 2009). As such it holds a prominent place in the body of research on fluid flow through deformed, porous media. This broader context includes a considerable body of research done by structural geologists and hydrogeologists alike.

Structural geologists tend to rely on surface field data like outcrop mapping, in situ permeametry, and fault zone architecture to develop conceptual models. For example, such studies have been conducted in faulted Mesozoic sandstones and mudstones near Moab, Utah (Antonellini and Aydin, 1994, 1995), particularly the Moab Fault (Davatzes and Aydin, 2005), and in faulted Eolian sandstones at Valley of Fire State Park, Nevada (Jourde et al., 2002).

Hydrogeologists, on the other hand, rely on subsurface field methods like mapping of horizontal and vertical hydraulic head gradients and pumping/injection testing. For example, such studies have been conducted in unconsolidated sediments in the Lower Rhine Embayment, Germany (Bense and Van Balen, 2004), Mesozoic sandstones in the Tucano Basin, NE Brazil (Medeiros et al., 2010), and faulted Paleozoic sedimentary rocks along the margins of the Rio Grande Rift, New Mexico (Haneberg, 1995). More examples of both surface and subsurface-based approaches are cited by Bense et al. (2013).

In recent years there has been a push for a more interdisciplinary approach to fault zone hydrogeology (Bense et al., 2013). This thesis and the larger SSFL characterization, while

largely employing traditional hydrogeological methods, also integrates some key surface-focused methods to develop the conceptual and numerical models. This, therefore, is a step toward such an interdisciplinary approach to faulted rock hydrogeology.

Chapter 2: SSFL Description

2.1 SSFL Overview

This section provides an overview of the background information about the SSFL that is important for the context of this thesis.

2.1.1 Geography

The SSFL is a complex of industrial research and development facilities located 30 miles NW of Los Angeles (Figure 2.1) and situated within Simi Hills which are part of California's Transverse Ranges geomorphic province. The area has high relief with a maximum elevation of ~2,000 ft (~600 m) asl, and ~1,100 ft (330 m) of topographic relief expressed within the property boundary (MWH, 2009). The SSFL is flanked by low-lying valleys containing the city of Simi Valley to the north and the communities of Chatsworth and the communities of Chatsworth, West Hills,

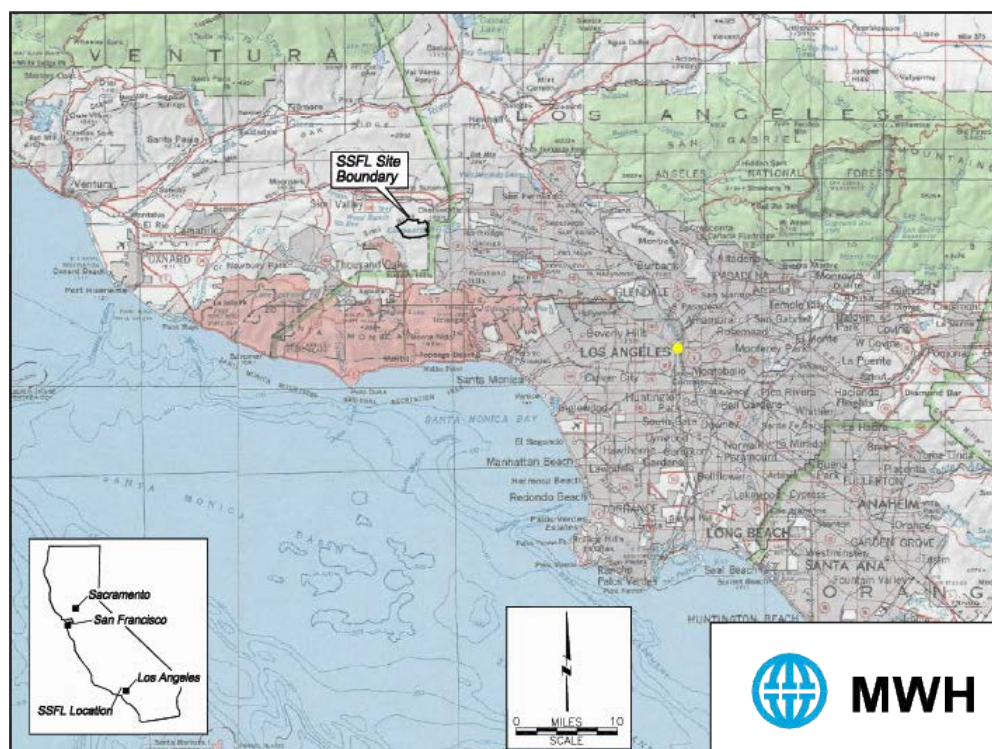


Figure 2.1 SSFL location map. (MWH, 2009)

and San Fernando Valley to the east. The property is bordered on the south by the Santa Monica Mountains (Cilona et al., 2016). The regional geographic setting is shown in Figure 2.2.



Figure 2.2 Regional setting of the SSFL. Also shown are the locations of Areas I-IV. (MWH, 2009)

2.1.2 Operations and Environmental Impact

The SSFL property covers a vast area of 2,850 acres and is divided into four administrative areas (Areas I, II, III, and IV) (Office of Inspector General, 2014). Ownership of these areas is divided among the Boeing Company (Boeing) and the U.S. National Aeronautics and Space Administration (NASA). NASA owns all of Area II and a 42-acre parcel of Area I. The rest of the site is owned by Boeing, but a portion of Area IV to was leased to the U.S. Department of

Energy (DOE) (Office of Inspector General, 2014). The study site for this thesis is within NASA's Area II property near the northern border of the SSFL property.

Activities began at the SSFL in 1948 and included research in nuclear energy by DOE and the development and testing of rocket engines by NASA (MWH, 2009). All activities had ceased by 2006, and the site has since been decommissioned. These operations resulted in radioactive and chemical contamination of the soil and groundwater (Office of Inspector General, 2014). The primary contaminant of concern (COC) is trichloroethylene (TCE), a chlorinated hydrocarbon used as a solvent to clean rocket engines (Office of Inspector General, 2014). Denser than water, TCE is a colorless, nonflammable liquid that has been linked to several adverse health conditions including cancer in humans (EPA, 2016).

2.1.3 Remediation Efforts

NASA began cleanup work at the SSFL in the early 1980s, but specific remediation requirements were not prescribed until 2007 when NASA, Boeing, and DOE signed consent orders with California's Department of Toxic Substances Control (DTSC) under the authority of the Resource Conservation and Recovery Act (RCRA). In this agreement, the entities agreed to clean up the groundwater and soil to residential exposure levels (Office of Inspector General, 2014).

The first official site-wide remedial investigation of the SSFL was submitted to DTSC in 2009 (MWH, 2009). This report was accompanied by a site conceptual model (SCM). These documents synthesized all existing geologic, hydrologic, and chemical knowledge about the SSFL. A diagram of the 2009 SCM is presented in Figure 2.3. The 2009 report concluded that even though groundwater advection occurs mainly within the fracture network, essentially all

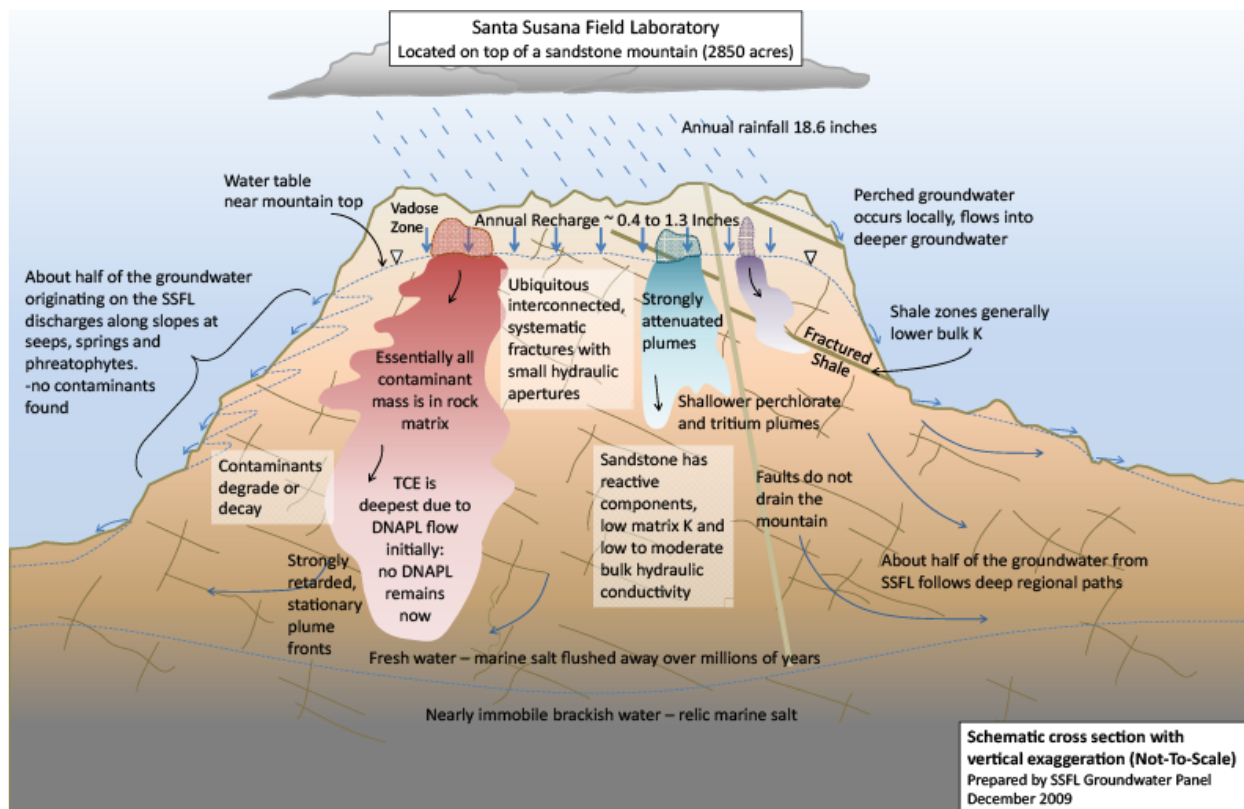


Figure 2.3. The 2009 local scale SCM. Not to scale. (MWH, 2009)

COCs have diffused into the rock matrix. Consequently, the reports asserted, COCs are not likely to migrate off-site and that the process of biologic attenuation will be a sufficient remediation technique.

These measures and conclusions, however, were not approved by DTSC. Furthermore, DTSC identified several data gaps where additional data would be necessary (National Aeronautics and Space Administration (NASA, 2017)). Several of DTSC's comments indicated that more data was needed to characterize the influence of faults and fine-grained units on groundwater flow and contaminant transport at critical remediation zones (NASA, 2014). Results of ongoing studies, including this thesis, will be used in the future to amend, if necessary, the conclusions reached by the 2009 reports.

2.2 Geology and Hydrogeology

Structural geology and stratigraphy have important influences on the hydrogeology of the SSFL. Therefore, geological characterization has been a critical part of remedial investigations at SSFL. The earliest cited geological characterization of the was a study of Cretaceous turbidites in the Simi Hills published in 1981 by Link et al. Mapping was done in 1992 by Dibblee. Atwater (1998) published a tectonic history of the Western Transverse Ranges. In 2007, as part of their remedial investigation, MWH published a geological characterization of SSFL which compiled all relevant existing research as well as additional work done by MWH. More recent studies of the faults and fracture patterns at SSFL have been done by Cilona (2014, 2016).

2.2.1 Chatsworth Formation

A geologic map of the Simi quadrangle from Dibblee (1992) is shown in Figure 2.4. As shown, the principle geologic unit at the SSFL is the Late Cretaceous Chatsworth Formation. The Chatsworth Formation is a deep-marine turbidite (Link et al., 1981) from a mid-fan environment. It consists of sandstone beds that are 1-30 ft thick interbedded with thinner shale and siltstone beds that are 1-3 ft thick. Less extensive lenses of conglomerate are also present within coarse-grained units and are generally less than 5 ft thick. Individual members are classified based on the frequency of fine and coarse beds. Locations of fine-grained outcrops within the Chatsworth Formation are shown in the geologic map in Figure 2.5, and a stratigraphic column of the Chatsworth Formation is shown in Figure 2.6. The total thickness of the Chatsworth Formation is unknown but is at least 6,000 ft thick. The upper Chatsworth Formation alone is nearly 4,000 ft thick (Cilona et al., 2016). These alternating beds dip to the NW between 25 and 30 degrees, consistent with the structure described in the previous section. The Chatsworth Formation is

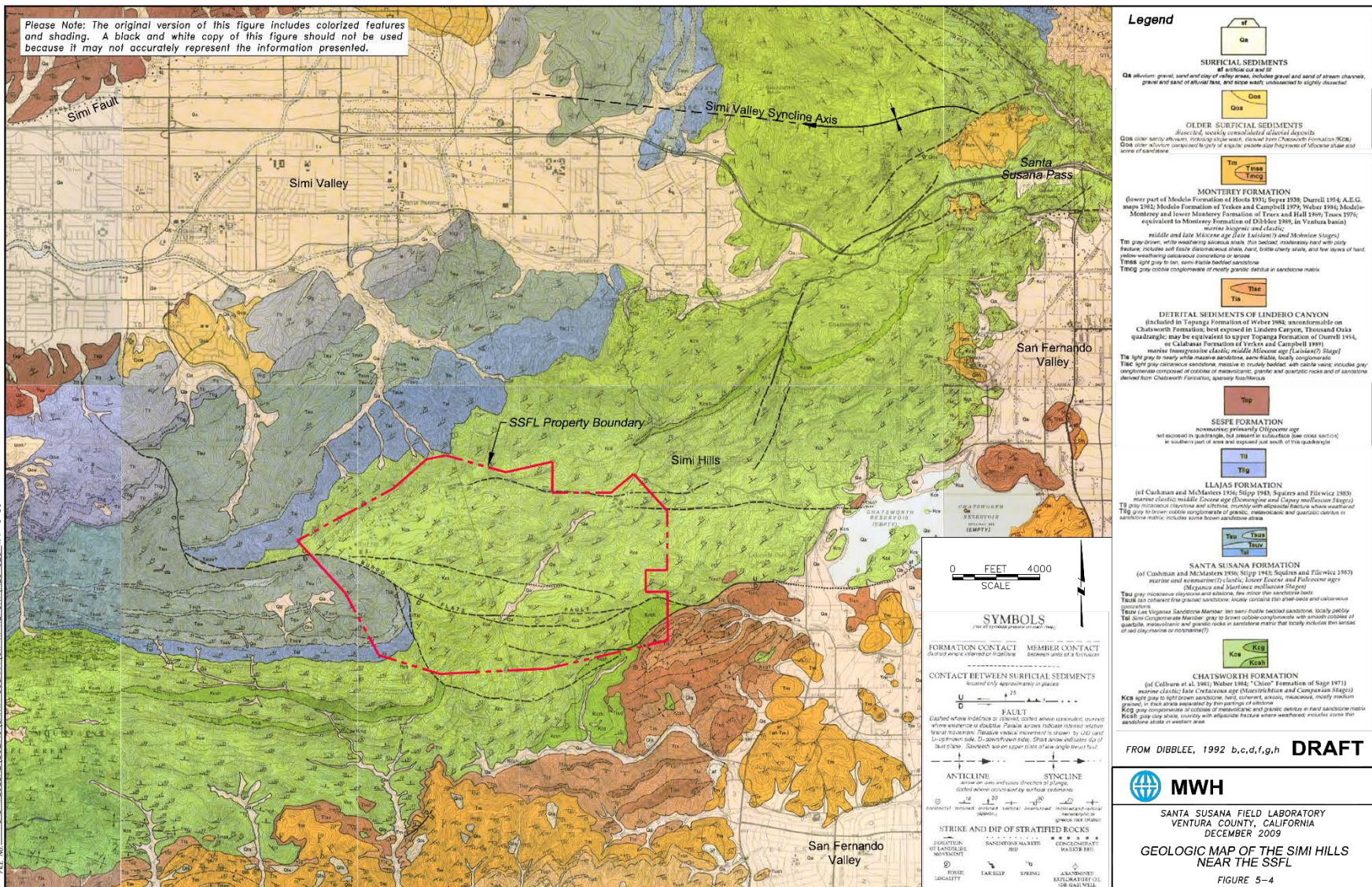


Figure 2.4 Geologic map of SSFL and surrounding region. The Chatsworth Formation is shown in green. (Dibblee, 1992)

FILE No. CAD, MALIBU, BOILING SANTA SUSANA LG, RI, REPORT, REC, GEO, MAP, 6 09

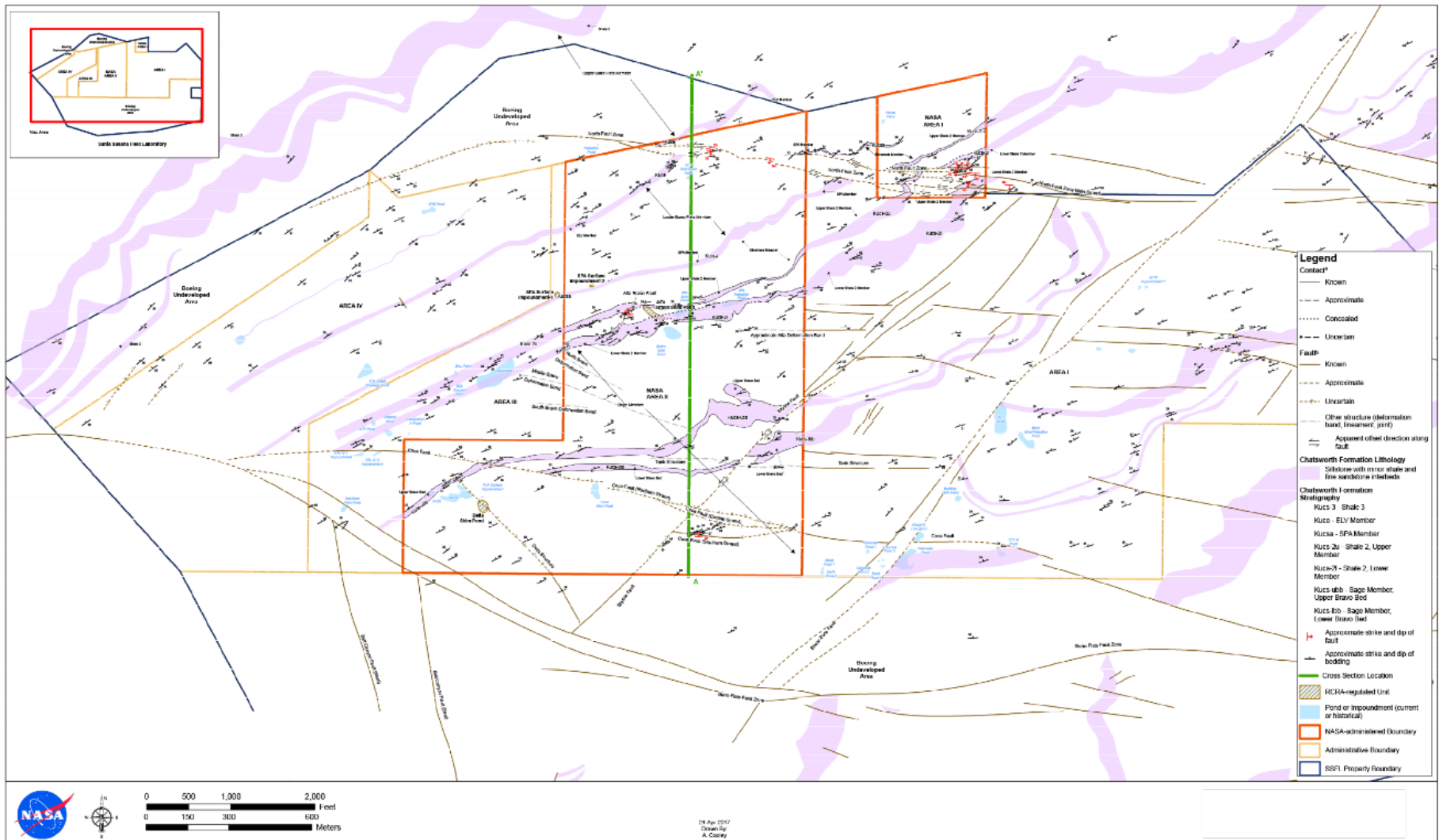


Figure 2.5 SSFL Chatsworth Formation map. Fine-grained members are shaded. The green line is the cross section line for figure 2.3-3. (NASA, 2016)

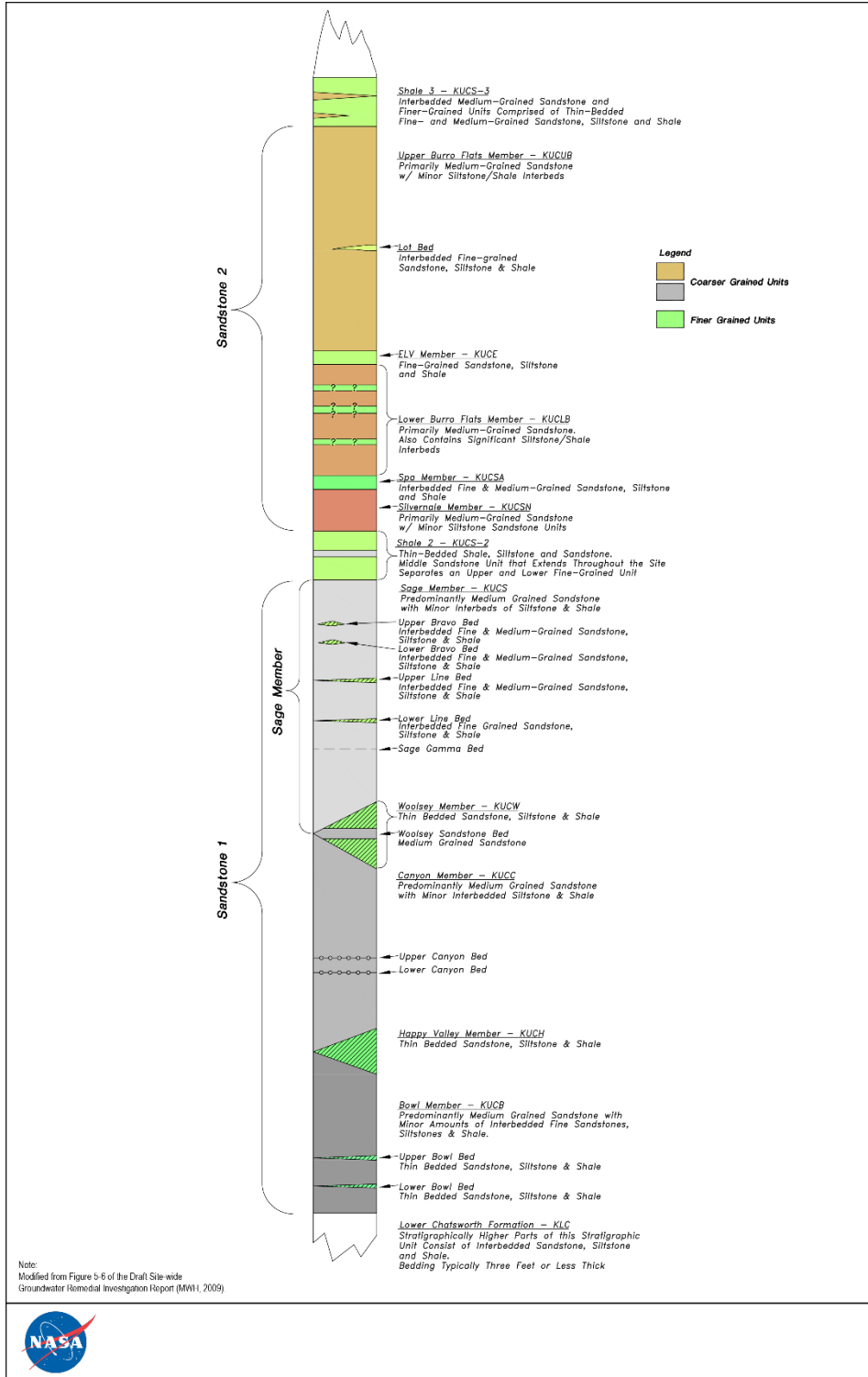


Figure 2.6 Stratigraphic column of the Chatsworth Formation. (NASA, 2016)



intensely faulted and fractured throughout which is also consistent with the structure described. The porosity of the Chatsworth Formation rock matrix is estimated to be ~14% (MWH, 2009)

2.2.2 Structural Geology

The Simi Hills are within the Transverse Ranges, a geomorphic province known for its structural complexity (Cilona et al., 2016; MWH, 2007; Atwater, 1998). Structurally, the region is in north-south compression (MWH, 2009). Sedimentary rock beds dip to the NW at ~30 degrees as depicted in the cross section in Figure 2.7. Figure 2.8, shows the orientation of the dominant fault sets at the SSFL. One set trends NE-SW and the other set trends ESE-WSW. Both sets have evidence of both strike-slip and dip-slip components (Cilona et al., 2016).

The complex structural history of the Western Transverse Ranges began in the Miocene (~15 Ma), when the Transverse Ranges began rotating. Since then it has rotated as much ~90 degrees clockwise due to right-lateral movement along the San Andreas Fault (Atwater, 1998). This phase was associated with shearing and extension of the Transverse Ranges. In the Plio-Pleistocene (~5 Ma), the stress regime changed again when the Baja block to the south began colliding with the Transverse Ranges. This phase is associated with the uplift, folding, tilting and faulting that is still occurring today (Atwater, 1998; MWH, 2007). As a result of this rich structural history, the rocks at SSFL are intensely fractured, and both bedding parallel and bedding normal fractures are ubiquitous (Cilona et al., 2016).

2.2.3 Hydrogeology

There are two hydrostratigraphic units at the SSFL. One of them is the Quaternary sediments that contain the near surface groundwater system. These sediments are up to tens of ft (>3 m) in some

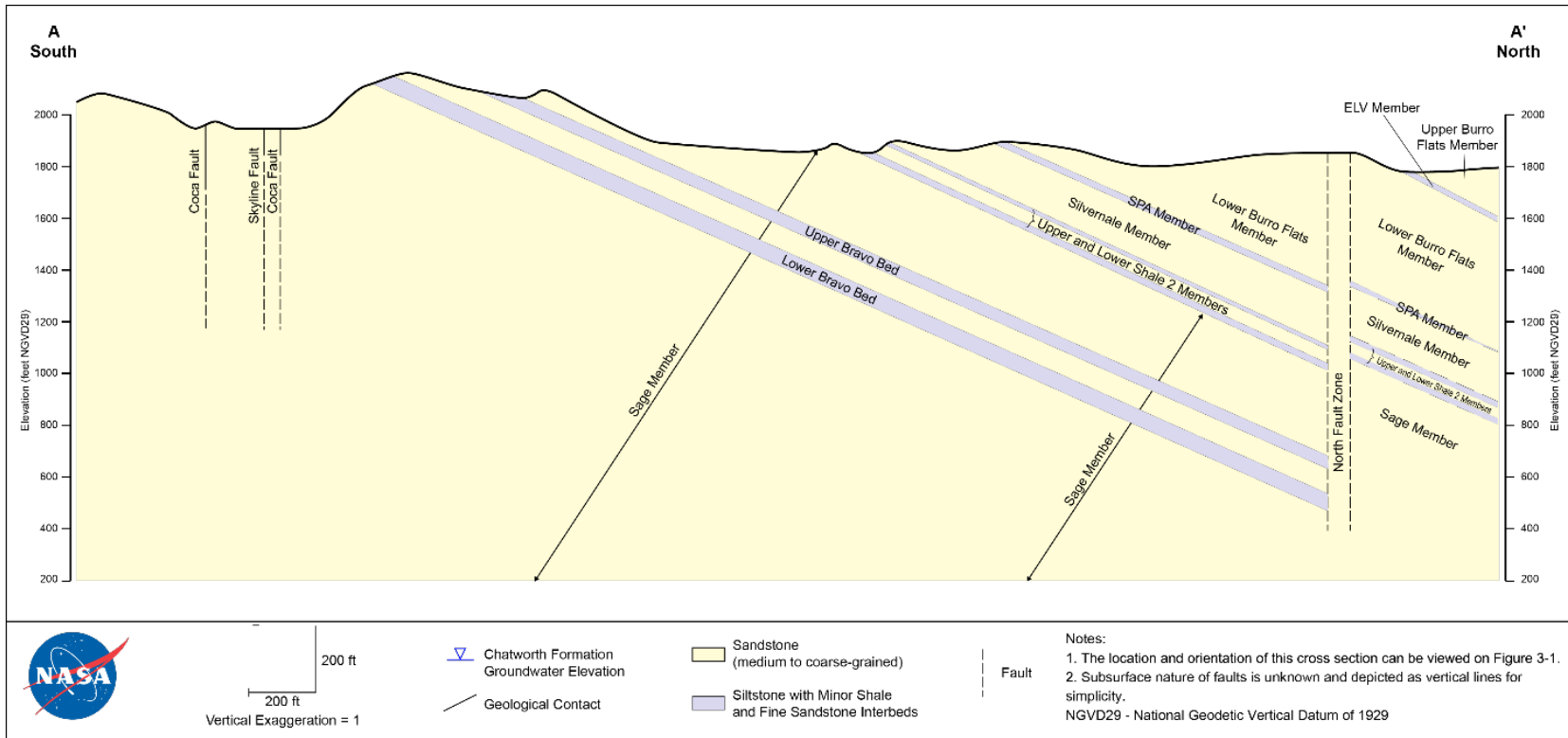


Figure 2.7 Cross section showing the general structure of the Chatsworth Formation. This cross section corresponds to the green line in figure 2.5. (from NASA, 2016)

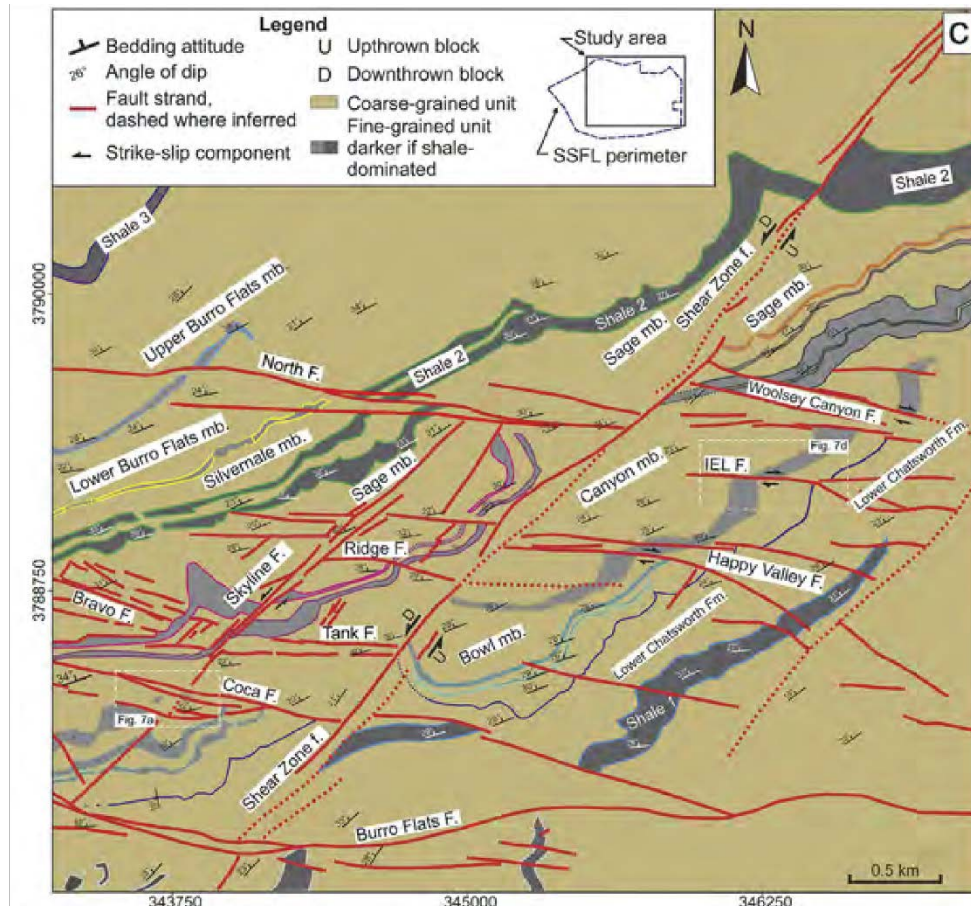


Figure 2.8 Map showing the two main fault orientations at SSFL, ESE-WNW and NE-SW. (Cilona et al., 2016)

places, but are not present everywhere at the SSFL (MWH, 2009). This groundwater system is only mentioned for reference and is not considered in this thesis. The other hydrostratigraphic unit, of course, is the Chatsworth Formation which is further subdivided into two subunits: Sandstone 1 and Sandstone 2 which are separated by Shale 2 (see stratigraphic column in Figure 2.6).

Groundwater recharge at the SSFL is from infiltration of precipitation (AquaResource/MWH, 2007). Annual precipitation is estimated to be ~18 in (457 mm), and infiltration is estimated to be anywhere from 12% to less than 1% of precipitation depending on

local topography and geology (AquaResource/MWH, 2007). General Groundwater flow directions at the SSFL are topographically controlled, flowing down the mountain and discharging at seeps, springs, and phreatophytes along natural hydrologic boundaries (MWH Americas, Inc., 2009). These boundaries are shown in Figure 2.9. The base of the active groundwater system is believed to be at 0 ft asl since little mixing with saline or brackish groundwater is expected to occur below that depth (AquaResource/MWH Americas, 2007).

The total porosity of the Chatsworth Formation is determined by the primary porosity of the sedimentary rock matrix and the secondary porosity of the fracture network. However, MWH (2009) found that the fracture network was several orders of magnitude smaller than the rock matrix porosity. Furthermore, Cilona et al. (2016) found that there was a high degree of connectivity within the fracture network in all directions including the vertical direction. They suggest that the fracture network could provide flow pathways across low permeability units within the Chatsworth Formation. Faults in the Chatsworth Formation generally act as hydraulic barriers. Studies of the Shear Zone Fault in the western SSFL conclude that shale smear along fault planes significantly decreases the permeability of the fault core (Cilona et al., 2014).

2.3 B204 Area and the North Fault Zone

Areas where COC plumes exist are designated as areas of impacted groundwater (AIGs). On the NASA side of the project, there are seven AIGs (NASA, 2017). The AIG that concerns this thesis is the Building 204 (B204) AIG located in Area II near the SSFL's northern boundary (see Figure 2.10). According to the most recent analyses, some COCs have been detected offsite seeps and springs north of the SSFL boundary near the B204 area, but these detections are sporadic and not consistent over time.

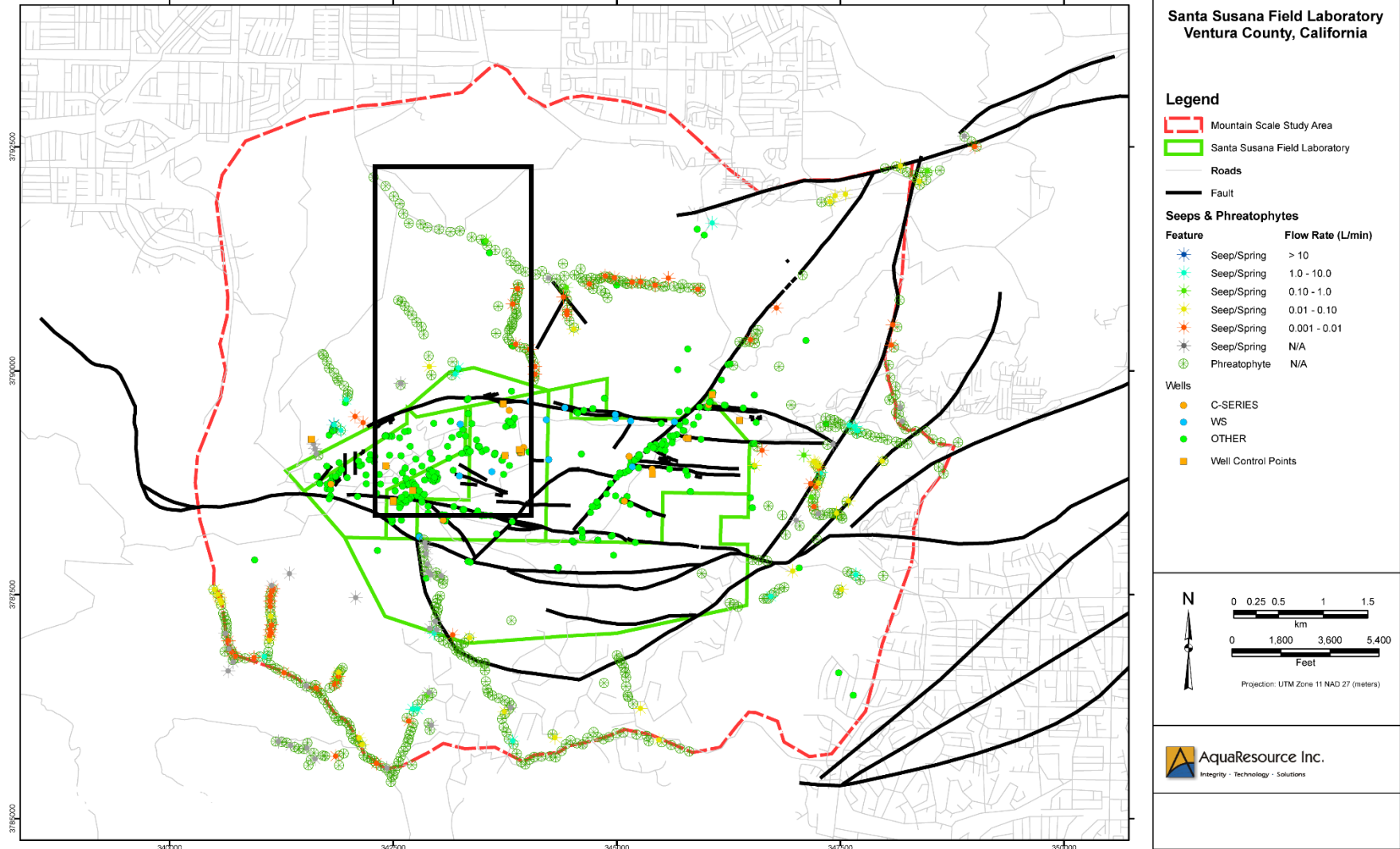


Figure 2.9 Mountain scale boundary condition map showing groundwater discharge locations. The Black box indicates where seeps, springs, and phreatophytes are mapped in drainages north of the SSFL boundary close to the B204 area. (AquaResource/MWH, 2007)

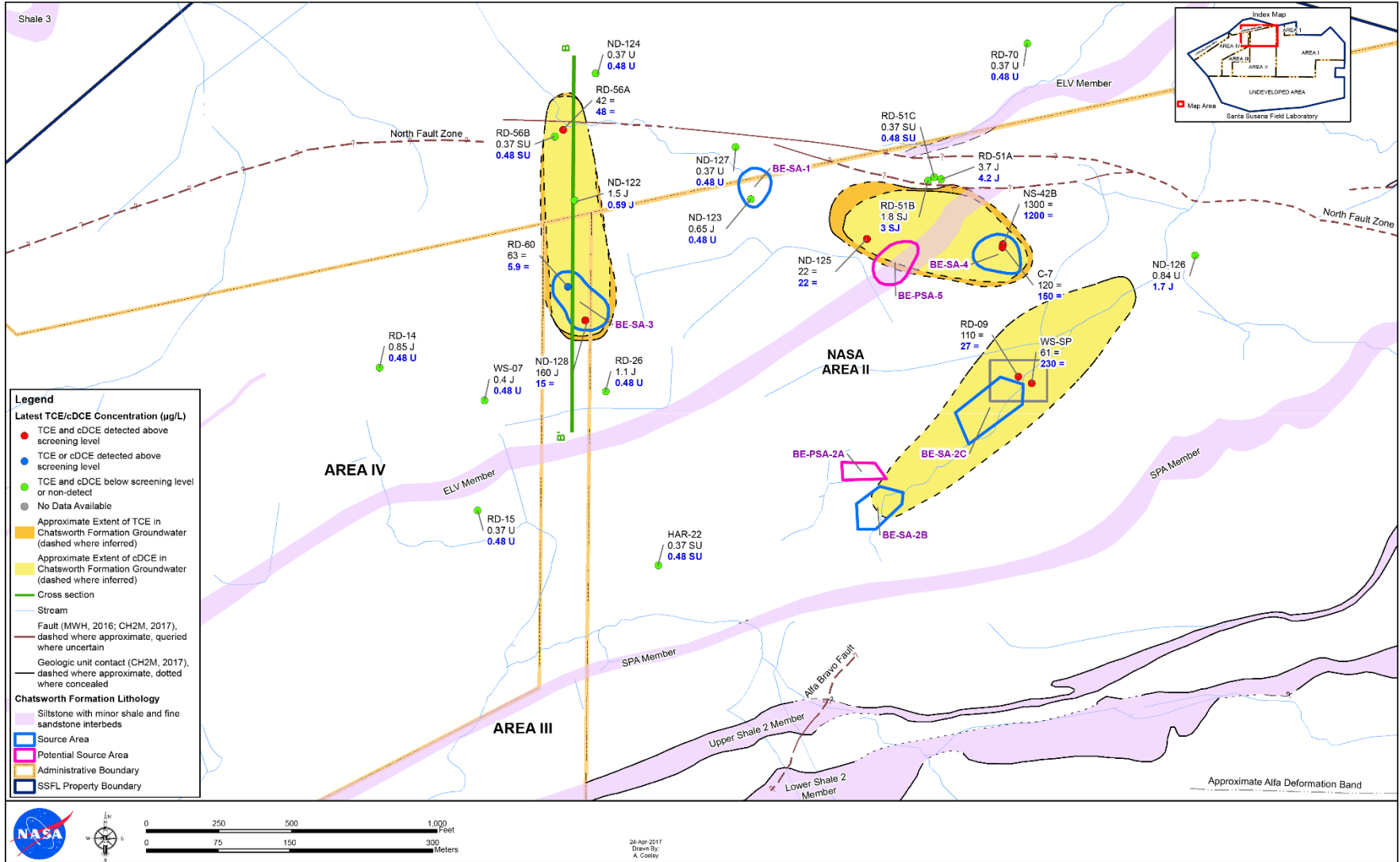


Figure 2.10 Map of the B204 and ELV areas. The cross section line for figures 2.11 and 2.13 is shown in green. (NASA, 2016)

2.3.1 Local Stratigraphy and Structure

The bedrock at the B204 area consists of the uppermost members of the Chatsworth Formation denominated as Sandstone 2 (see stratigraphic column in Figure 2.6). Most important are the Upper Burro Flats Member, the ELV Member, and the Lower Burro Flats Member. Other less important members are the SPA and Silvernale Members. North of the SSFL boundary, the Chatsworth Formation concludes with its upper most Member, Shale 3. Further to the north, Shale 3 gives way to the younger Simi Formation. These units follow the regional structure dipping to the NW at ~30 degrees. The Upper and Lower Burro Flats Members and the Silvernale Member consist primarily of sandstone. All three have some interbedded siltstone and shale but the Lower Burro Flats has significantly more than the other two. The ELV and SPA Members are primarily interbedded shale, siltstone, and fine sandstone.

The primary geologic structure near the B204 area is the North Fault Zone (NFZ) which is a cluster of E-W striking faults. The faults are believed to have left-lateral strike-slip with a minor normal dip-slip component (MWH, 2007). A measurement of a fault slip surface with slicken lines suggests that at least one of the major faults dips at ~60 degrees to the south (NASA, 2014). This subsurface structural relationship between the bedding and the faulting is shown in the cross section in Figure 2.11. Figure 2.11 also shows fracture orientations measured in well boreholes across the B204 area. The fracture orientations are complex with both bedding parallel and bedding normal fracture sets present.

2.3.2 Groundwater Elevations

Figure 2.12 shows Chatsworth Formation groundwater levels near the B204 area. The horizontal gradient shows that flow is generally N-S. The cross section in Figure 2.13 shows water levels in

the vertical dimension. This cross section follows a well transect running the length of the B204 COC plume, crossing the NFZ, and terminating at a well cluster at the SSFL boundary. This transect includes wells screened within the Upper and Lower Burro Flats Members. These water level measurements indicate that in the vertical direction, flow behavior is more complicated than in the horizontal plane. South of the NFZ, water levels at wells ND-122, RD-60, and ND-128 indicate that heads in the Upper Burro Flats are slightly higher than heads in the Lower Burro Flats. North of the NFZ, water levels at well screens above the ELV (RD-56A-1,2) are up to 200 ft lower than in wells screened below the ELV (RD-56B). It is apparent that heads in the Upper Burro Flats drop precipitously across the NFZ while heads in the Lower Burro Flats do not exhibit such a drop. Consequently, there is a reversal of vertical head gradient across the NFZ.

The cross section in Figure 2.13 includes a representation of the B204 COC plume. The shape of this plume is an interpretation based on groundwater sampling results (NASA, 2017). It is apparent that contaminants have migrated vertically downward into the Lower Burro Flats south of the NFZ and have reentered the Upper Burro Flats north of the NFZ. The shape of the B204 plume gives some insight into the flow dynamics. This will be discussed further in chapter 4.

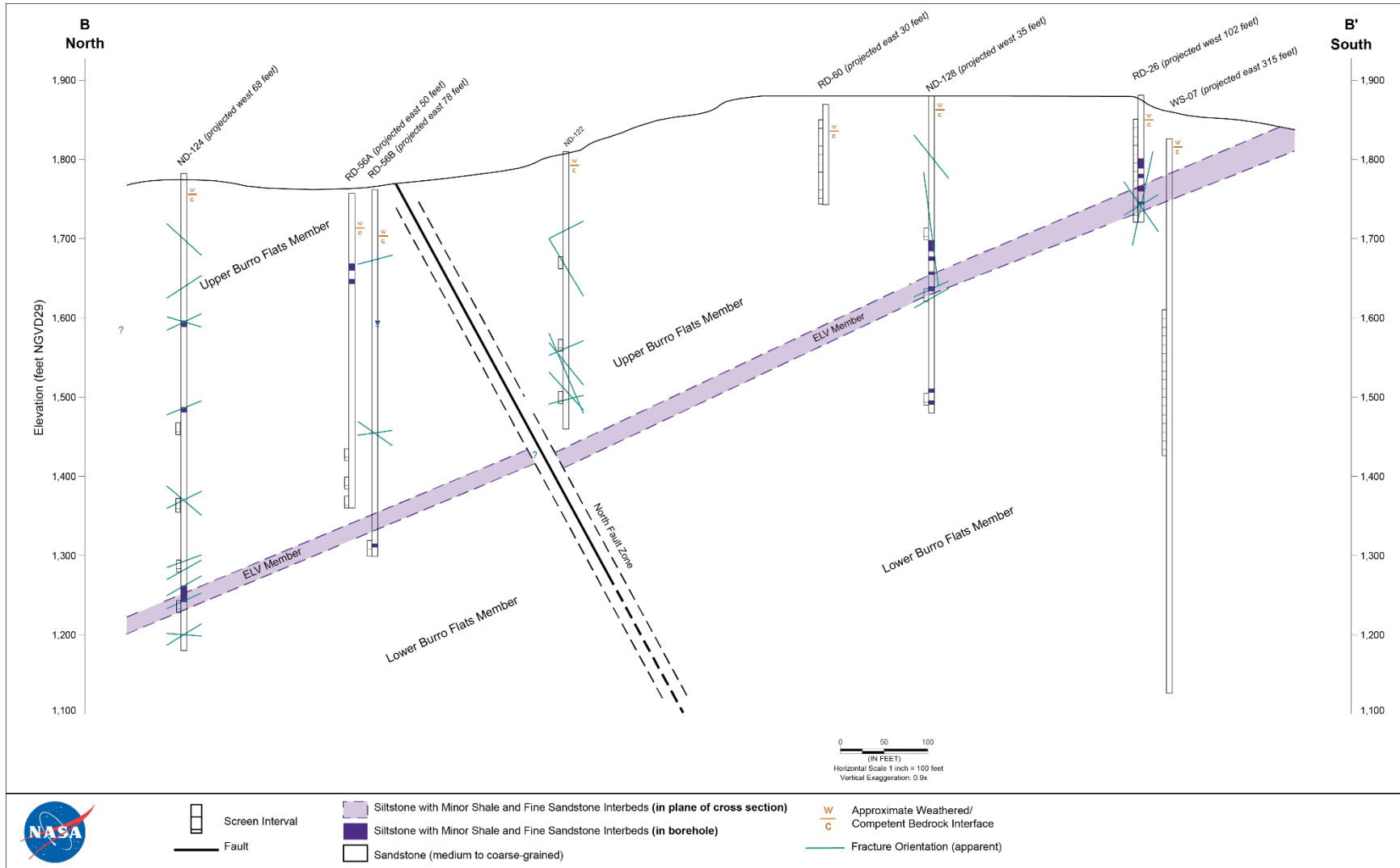


Figure 2.11 Geologic cross section of the B204 area showing structural the structural relationship of the NFZ and the stratigraphic units. The cross section line is shown in figure 2.10. (NASA, 2016)

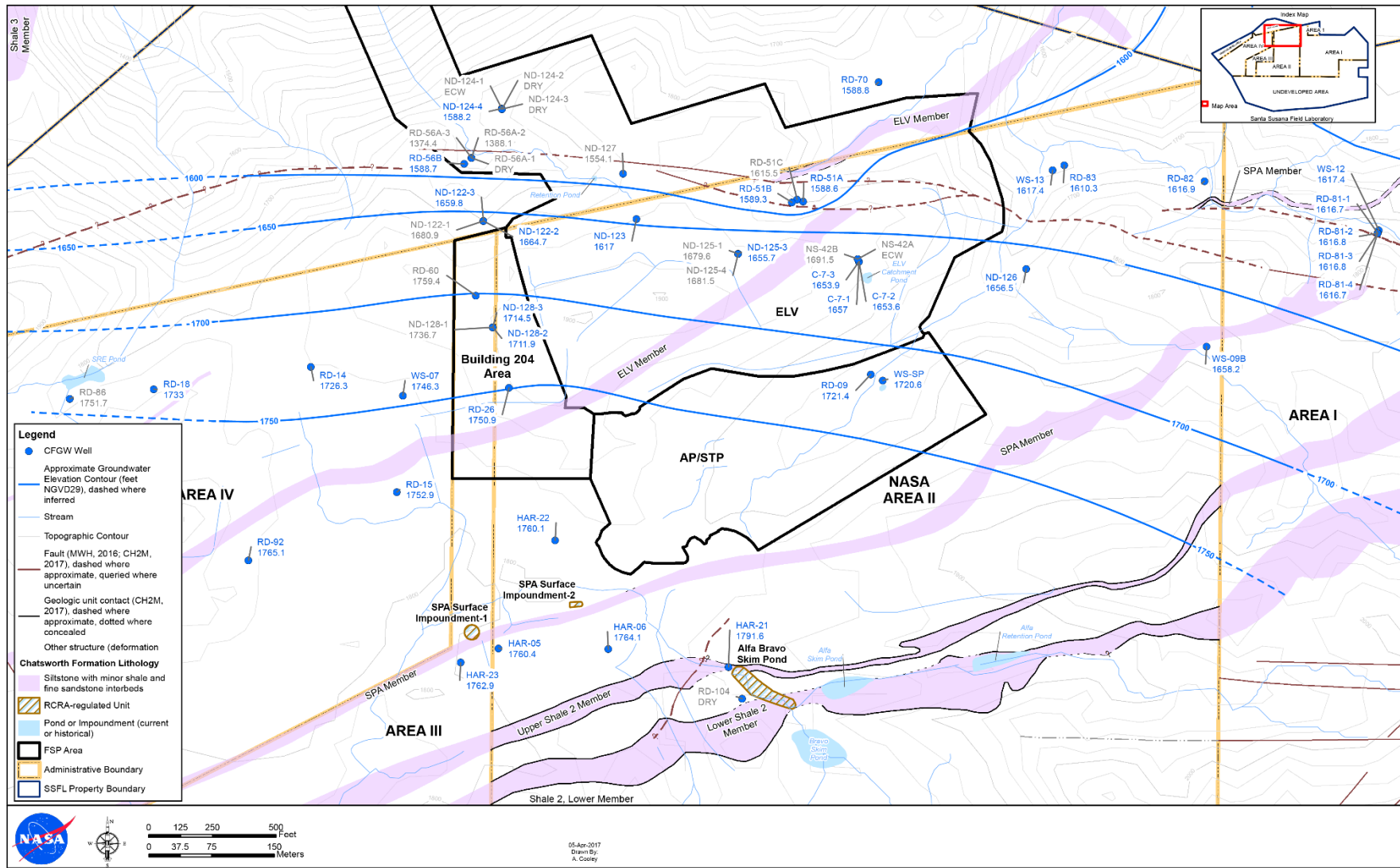


Figure 2.12 Groundwater elevation map of the B204 and ELV areas. Water elevation contours show the uniform N-S flow direction. (NASA, 2016)

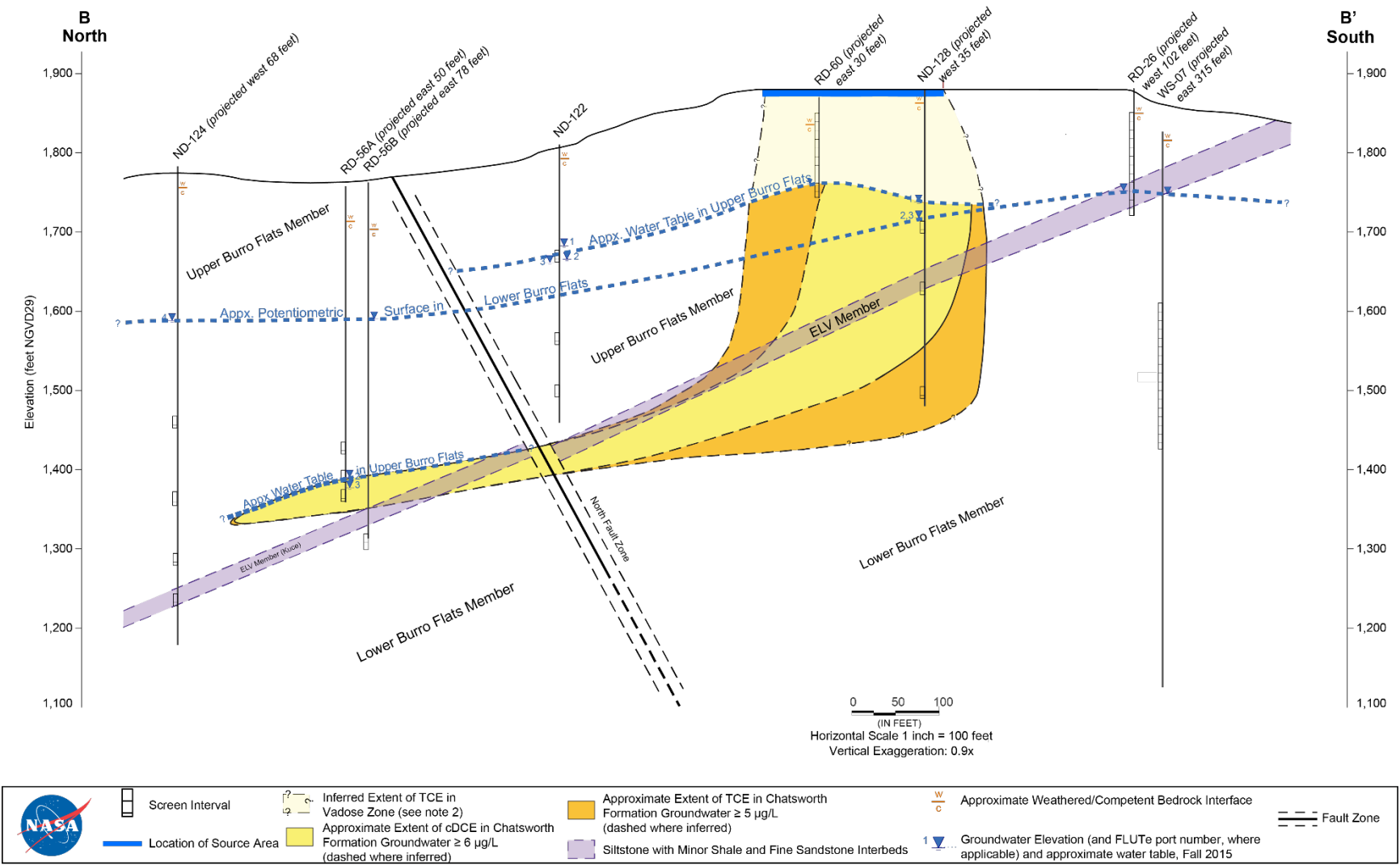


Figure 2.13 Hydrogeologic cross section of the B204 area showing the complex nature of the vertical groundwater flow system. This cross-section corresponds to the green line in figure 2.10. (NASA, 2016)

Chapter 3: Modeling Methods

3.1 Overview of Objectives and Methods

The objective of this thesis is to investigate, through the process of numerical modeling, the following questions relating to the groundwater system at the at the B204 AIG:

1. What key features control groundwater flow at the B204 area?
2. What are the causes of the large drop in head across the NFZ?
3. Why does this head-drop occur only in the Upper Burro Flats Member?

The process for modeling fluid flow in fractured rock is described in detail by the Committee on Fracture Characterization and Fluid Flow (1996). The process consists of formulating a conceptual model and a mathematical model, synthesizing them into a hydrogeological simulation model, calibrating this model to field observations and measurements, and using simulation results to refine the conceptual model. An illustration of this process is shown in Figure 3.1. In the conceptual model, various hypotheses concerning key hydrogeologic features are presented. The mathematical model presents the flow equations and numerical methods used to construct the simulation model. The simulation model is then used to evaluate the hypotheses presented in the conceptual model by calibrating the simulation model by altering model parameters over several simulation runs. The data used for model calibration were water level measurements from the wells along the B204 transect. These measurements were made by CH2M Hill geologists during groundwater monitoring in May 2016. Several of the wells in the transect are developed as multilayered wells using FLUTE® liners to isolate depth intervals and obtain groundwater measurements at several depths within a single borehole (NASA, 2014). These data are used with the permission of CH2M Hill and NASA.

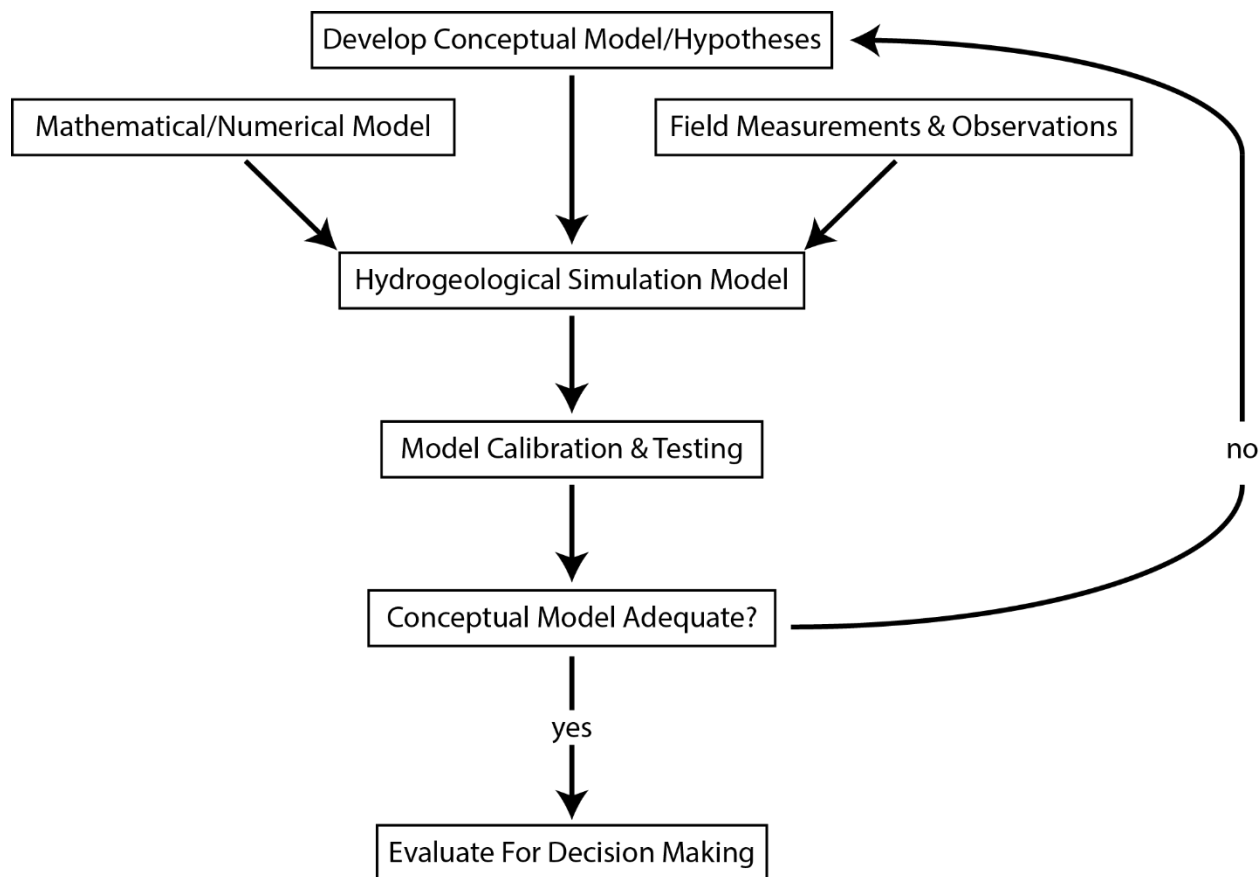


Figure 3.1 Flow chart illustrating the modeling process. (adapted from CFCFF, 1996)

3.2 Conceptual Model

The development of a conceptual model for groundwater flow is really the development of one or more hypotheses to explain the observed flow phenomena. It is an iterative process in which the conceptual model is constantly revisited and refined as the hypotheses are either accepted or rejected. This section defines the hypotheses that were developed for testing. Developing a conceptual model involves identifying the key elements of the system and conceptualizing how they behave within that system. In deformed rock, key features usually consist of structural features like faults and highly transmissive fractures or fracture sets. The key features at the B204 site are water budget, the NFZ, the hydrostratigraphic units, and the fracture network.

3.2.1 Recharge and Discharge Conceptualization

The conceptualization of the recharge and discharge is important because it is ultimately what determines where water enters and exits the model. At the B204 area, it is well established that groundwater flows from south to north. Therefore, recharge must occur to the south, and discharge must occur to the north. The only means of recharge at B204 is infiltration of precipitation. Infiltration rates may vary; however, rates tend to be lower over inclined surfaces and where less permeable rocks outcrop. Recharge values are assigned based on known precipitation and infiltration rates for the B204 area described in section 3.4.2. For discharge, although no perennial streams are found near B204, there are seeps, springs, and phreatophytes mapped in drainages to the north indicating that all discharge is consumed by evapotranspiration. The steady state water budget conceptualization is as follows: recharge occurs at the surface at topographic highs by means of infiltration of precipitation, and discharge occurs at the surface at topographic lows by means of evapotranspiration.

3.2.2 NFZ Conceptualization

The conceptualization of the NFZ is perhaps the most critical element of this thesis. Generally, faults can act as either hydraulic conduits or hydraulic barriers (Bense et al., 2013). A large offset in water level across a fault, such as the one observed at the B204 area, is usually indicative that the fault is a hydraulic barrier. This is common in alternating sandstone and shale successions due to shale smear, grain reorientation, and gouge development along fault planes which also tends to impose fault parallel anisotropy within fault zones (Bense and Person, 2006). Other faults at the SSFL have exhibited similar behavior (Cilona et al, 2014). However, the fact that the large water table offset is either not present or not as pronounced in the Lower Burro Flats suggests that the NFZ is much more permeable below the ELV than above the it. To summarize, the two competing hypotheses that emerge are (1) the NFZ is a barrier to flow for

both the Upper and Lower Burro Flats Members and (2) the NFZ is a barrier to flow in the Upper Burro Flats Member but only a partial barrier to flow in the Lower Burro Flats Member.

3.2.3 Hydraulic Conceptualization

The hydraulic conceptualization defines the features of the flow system that effect the ability of the rock mass to transmit water. These features are the permeability of the stratigraphic units and the fracture network. Generally, hydrostratigraphic units can be classified as either conductive to groundwater flow (aquifer) or resistant to groundwater flow (aquitard). Generally speaking, coarse-grained rocks like sandstones are more conductive than fine-grained rocks like shales. The key consideration in conceptualizing hydrostratigraphy is scale. For example, a sandstone may have fine-grained heterogeneities that are important at the small scale but that do not need to be specifically represented at a larger scale. At B204, the sandstone units (Upper Burro Flats, Lower Burro Flats, and Silvernale Members) are considered aquifers despite having significant interbedding of shale and siltstone. The siltstone/shale units (ELV and SPA Members) are considered aquitards despite the presence of fine and medium grained sandstone beds (MWH, 2009; NASA, 2017). The effect of this interbedding is bedding parallel anisotropy such that conductivity to flow is greater in the direction parallel to bedding than in the direction normal to bedding. At the scale of this model, this conceptualization is considered appropriate.

Another element of the hydraulic conceptualization is the fracture network. At B204, both bedding parallel and bedding normal fracture sets are present. The main consideration in conceptualizing the fracture network is the degree of hydraulic connectivity between these two fracture sets. If there is limited connectivity within the fracture network, groundwater flow paths would likely be more heavily influenced by the anisotropy of the rock matrix permeability. If there is significant connectivity, as suggested by Cilona (2016), fractures may provide vertical flow paths across flow resistant heterogeneities. To summarize, the competing hypotheses that

emerge are (1) fractures have limited hydraulic connectivity and flow is dominated by the rock matrix permeability and (2) fractures are strongly connected and provide an isotropic permeability structure.

3.3 Mathematical Model

The mathematical model is considered first because many of the mathematical concepts serve as a construct for important elements of the conceptual model. The key elements of developing a mathematical model include selecting a model class, also referred to as a study approach, identifying the governing flow equations, and employing some mathematical method of solving the equations.

3.3.1 Study Approach

There are generally two main study approaches for simulating flow through fractured rock. These are the continuum approach and the discrete fracture network (DFN) approach (Hsieh, 1998). The continuum approach treats the fracture porosity as an equivalent porous medium (EPM) where fractures are analogous to pores and blocks are analogous to grains (Hsieh, 1998). If the blocks are porous, as in the case of the SSFL, a double-porosity may be necessary since the interaction between pores and fractures influences the temporal component of flow. However, in a steady state model, there is no temporal component, so a double porosity model is not necessary.

The DFN approach represents fractures as one- or two-dimensional features within a two- or three-dimensional continuum each with a specified transmissivity. For this approach, there is usually insufficient structural data to replicate the actual fracture network, so fracture networks are generated stochastically (Hsieh, 1998). Illustrations of the continuum and DFN approaches

are given in Figure 3.2. According to Hsieh (1998), the choice of either approach is not the key issue but rather the level of heterogeneity that is incorporated into the model.

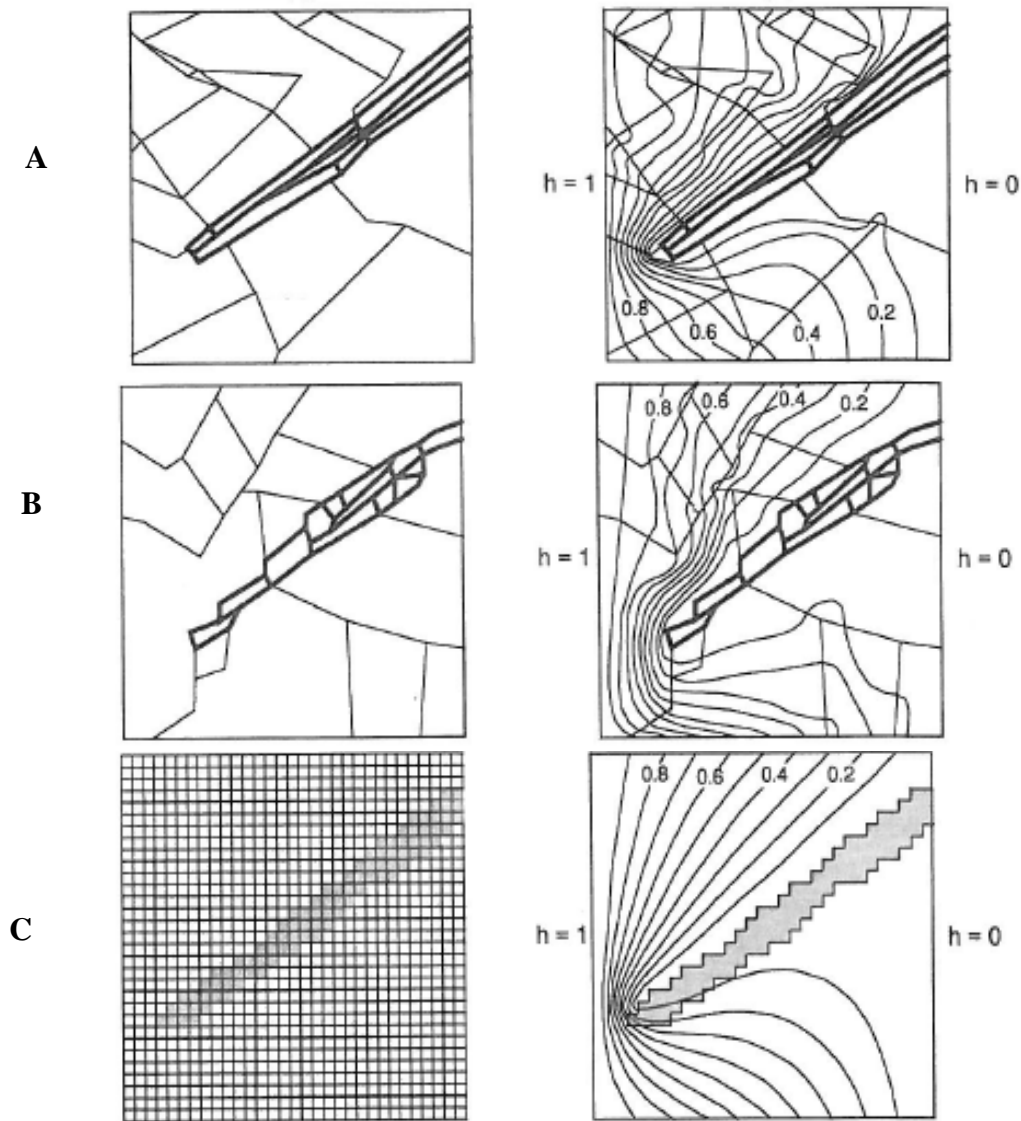


Figure 3.2 Illustrations of the two main study approaches for fracture flow modeling. The real fracture network (A) is simulated by a stochastic DFN approach (B) and a continuum approach (C). In all three figures head (h) decreases from 1 on the left to 0 on the right (units ambiguous). (Hsieh, 1998)

A critical element in defining the study approach is the dimensionality of the model. Both DFN and continuum models can be either two- or three-dimensional. Recall that in the B204 area, steady-state flow directions in two-dimensional plan view are essentially unidirectional. Therefore, expansion to three dimensions would likely not provide a significant advantage and

would greatly increase the complexity of model construction. Hence, this model is conceptualized as a two-dimensional cross section continuum model.

3.3.2 Governing Equations

The basic equation governing groundwater flow, Darcy's Law is as follows:

$$q = -K\nabla h \quad (1)$$

where:

q = specific discharge (L/T) defined as the volumetric discharge (L^3/T) per unit area (L^2) normal to flow

K = hydraulic conductivity (L/T)

∇h = hydraulic gradient defined as change in hydraulic head (h) over distance (x , y , or z)

In a steady state scenario, the law of conservation of mass can be expressed as:

$$-\left(\frac{\partial \rho q_x}{\partial x} + \frac{\partial \rho q_y}{\partial y} + \frac{\partial \rho q_z}{\partial z}\right) = 0 \quad (2)$$

where:

ρ = fluid density

q_x, q_y, q_z = components of the volumetric discharge

If Darcy's Law and steady state conservation of mass are combined and density assumed to be constant, the result is the groundwater continuity equation:

$$\frac{\partial}{\partial x} \left(K_x \frac{\partial h}{\partial x} \right) + \frac{\partial}{\partial y} \left(K_y \frac{\partial h}{\partial y} \right) + \frac{\partial}{\partial z} \left(K_z \frac{\partial h}{\partial z} \right) = 0 \quad (3)$$

Equation 3 is the governing equation for saturated steady flow, and applies to the portion of the subsurface below the water table. For steady-state unsaturated flow above the water table, the governing equation is the steady-state form of Richards Equation:

$$\frac{\partial}{\partial x} \left(K_x(\theta) \frac{\partial h}{\partial x} \right) + \frac{\partial}{\partial y} \left(K_y(\theta) \frac{\partial h}{\partial y} \right) + \frac{\partial}{\partial z} \left(K_z(\theta) \frac{\partial h}{\partial z} \right) = 0 \quad (4)$$

where:

θ =water content

In the Richards Equation, hydraulic conductivity becomes function of water content. The solution to the Richards Equation requires some sort of relationship between the saturation or water content and the hydraulic conductivity. Several such relationships have been conceived, each with its own set of assumptions. The one used here is a modified version of the van Genuchten relationship:

$$s_e \equiv \frac{(s-s_r)}{(s_s-s_r)} = \begin{cases} [1 + (-\alpha\psi)^n]^{-m}, & \psi < 0 \\ 1, & \psi \geq 0 \end{cases} \quad (5)$$

$$K_r = s_e^\delta \quad (6)$$

where:

s =saturation $\left(\frac{\text{fluid volume}}{\text{void volume}}\right)$

s_r =residual saturation $\left(\frac{\text{fluid volume}}{\text{void volume}}\right)$

s_s =maximum saturation $\left(\frac{\text{fluid volume}}{\text{void volume}}\right)$

s_e =effective saturation $\left(\frac{\text{fluid volume}}{\text{void volume}}\right)$

ψ =pressure head

α, m, n, δ =fitting parameters

K_r =relative conductivity

(Diercsh, 2014)

For this study, obtaining accurate values for s_s and the fitting parameters α , m , n , and δ was not necessary. A sensitivity analysis was conducted to determine the effect of the parameter on the water table elevation. This analysis revealed that these parameters only affect the saturation conditions above the water table but do not have a significant effect on the elevation or shape of

the water table. Values for these parameters were selected to facilitate the convergence of the numerical solution. The parameter values can be found in Table 3.1.

Table 3.1 van Genuchten parameters

Porosity	0.14
S_s	1
S_r	0.35
α	1
n	2
m	0.2
δ	1

3.3.3 Finite Element Method

Solutions to the flow equations presented above are difficult to obtain, especially for the highly nonlinear Richards Equation. Analytical solutions are typically only possible for highly simplified scenarios if they are possible at all. Numerical methods for solving these equations involve discretizing the model domain into a mesh and solving the equations at every node in the mesh simultaneously thereby approximating the solution numerically. Several mathematical formulations have been developed for numerical solution, each with its advantages and disadvantages. Modeling software packages are typically based on one of these methods. For example, the widely used MODFLOW software is based on the finite difference method (FDM). For this thesis, the software selected was FEFLOW which is based on the finite element method (FEM). The mathematical theory behind the FEM is beyond the scope of this thesis but can be found in Diersch (2014). The primary advantage of the FEM compared to the FDM is the greater flexibility of mesh construction. Figure 3.3 shows an example a finite element mesh. This increased flexibility is useful for representing features like faults and fracture.

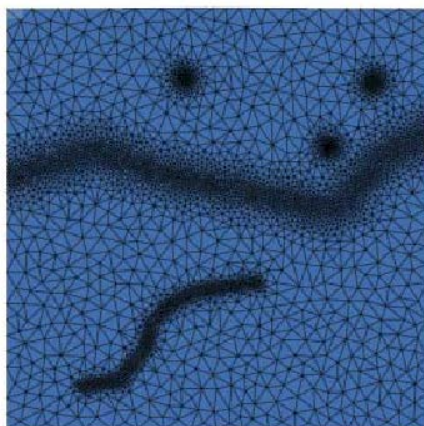


Figure 3.3 Example of a finite element mesh highlighting the flexibility of mesh discretization. (DHI, 2016)

3.4 Simulation Model Design and Calibration

The B204 simulation model was built to test the various hypotheses presented in the conceptual model. This section describes how the simulation model was constructed, how the various elements of the conceptual model were simulated, and how the hypotheses were evaluated.

3.4.1 Model Construction

The geometry and boundary conditions of the B204 simulation model are illustrated in Figures 3.4 and 3.5. Model boundaries were set at natural hydrologic features to approximate real conditions as much as possible. The model is constructed as a 2-D cross-section follows an idealized groundwater flow path. The cross-section line begins at the Shale 2 outcrop south of B204 and runs along the B204 plume transect northward to the RD-68 well cluster. Thereafter the line bends to the NW to follow a NW-SE drainage, and terminates at a larger NE-SW drainage. It should be noted that this northern extent of the cross section almost certainly receives groundwater flow from the east and west due to the higher topography off-section. This additional flow into the model is not accounted for, however, it is far enough removed from the critical elements of the flow regime that its influence is assumed negligible. The total length of the model is 7351 ft (2240.6 m). The upper boundary follows the topographic profile. The lower

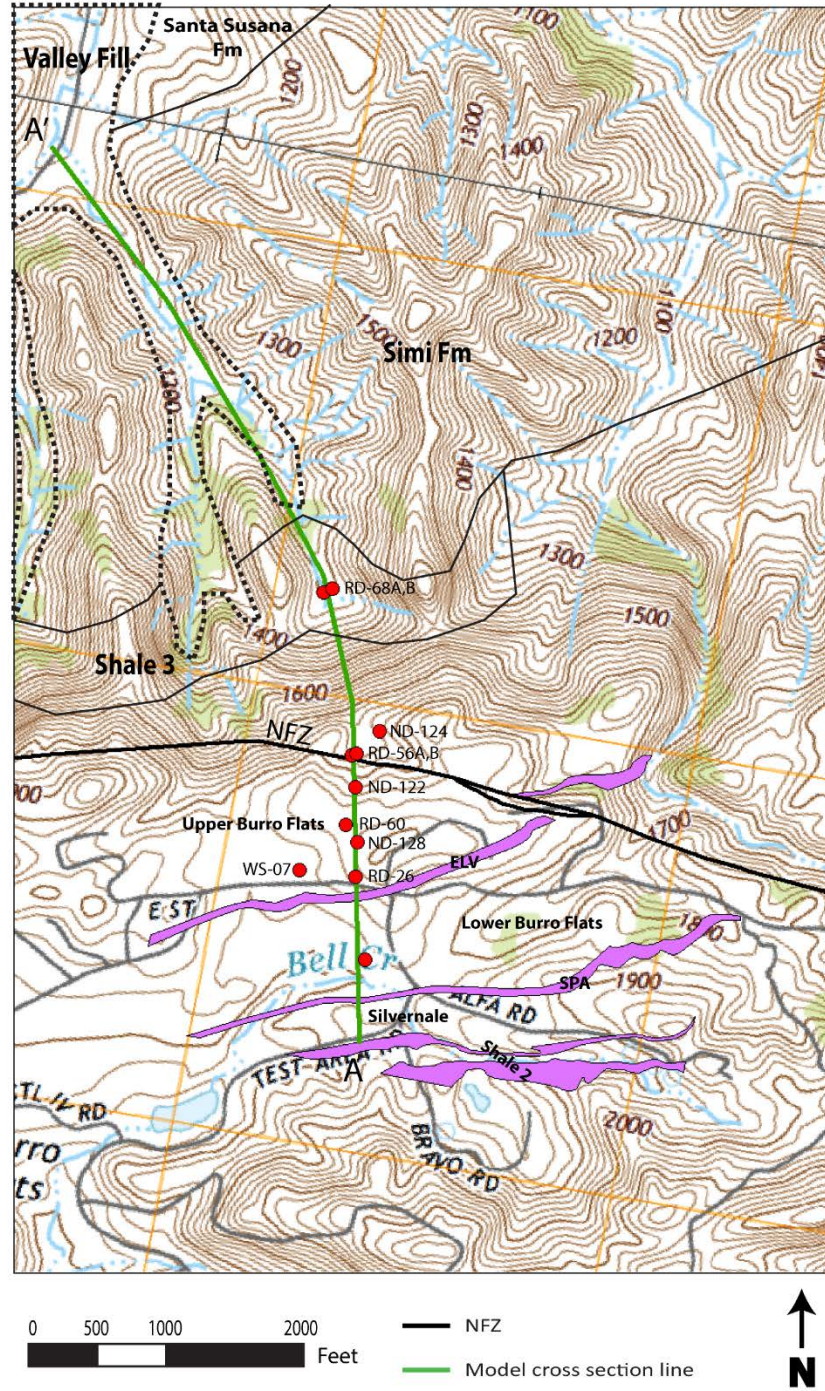


Figure 3.4 Topographic map showing the model cross section line in relation to geologic units and monitoring wells. (adapted from AquaResource/MWH, 2007)

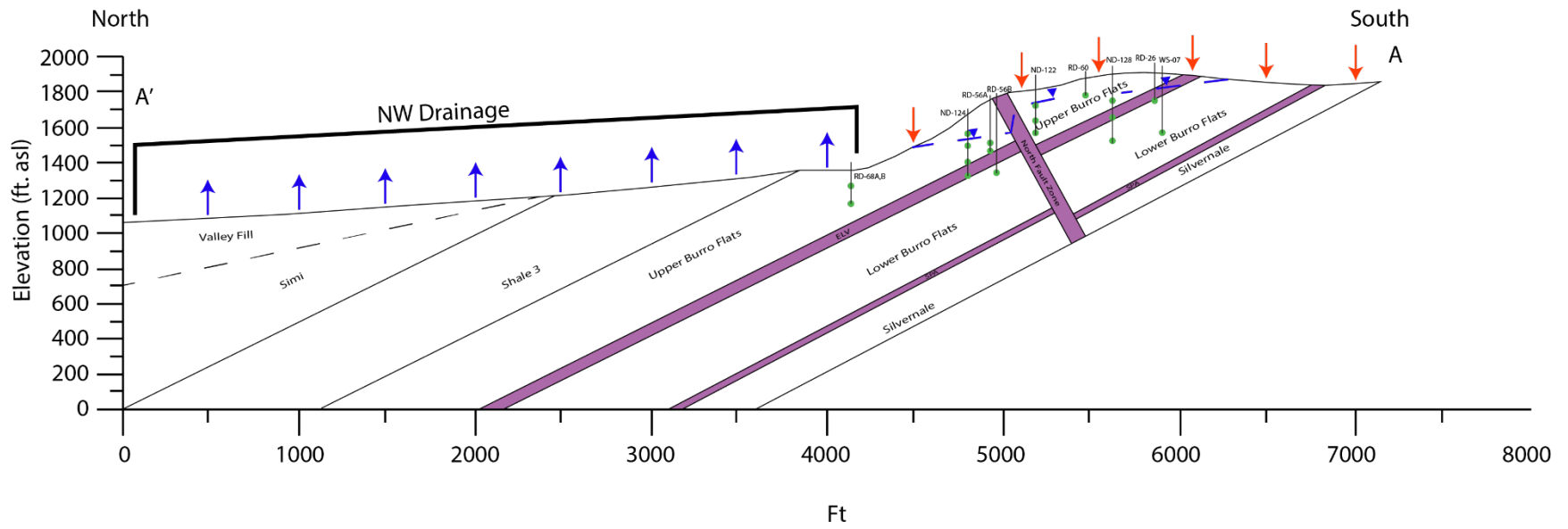


Figure 3.5 Diagram of the simulation model cross section.

boundary corresponds to the base of the active groundwater system which is assumed to be at sea level (0 ft. asl). The southern lateral boundary follows the dip of the Shale 2 contact. Observation points were placed to simulate well screens.

For conductivity zones, the model was divided into 12 conductivity zones as depicted in Figure 3.5. The Silvernale, SPA, ELV, Upper Burro Flats, and Lower Burro Flats were all divided into northern and southern sections with the NFZ as the divider. The NFZ was divided into an upper and a lower zone with the divider being the base of the ELV. The northern extent of the cross section includes shale 3

The tools available for model construction were fairly rudimentary and, therefore, are potential sources of error. The surface profile was created in Google Earth. The model was built within FEFLOW using existing maps and cross-sections of the B204 area to constrain geometry of the NFZ and the hydrostratigraphic units and the location of well screens as much as possible.

3.4.2 Boundary Conditions

Boundary conditions were assigned to simulate processes at the natural hydrologic features that create the model boundaries. Boundary conditions are illustrated in Figure 3.5. At the southern boundary, the dipping shale bed is assumed to be an aquitard. Therefore, this boundary is considered a no-flow boundary. The lower boundary at the assumed interface between fresh and brackish groundwater is also considered a no-flow boundary since no mixing occurs at that boundary. The upper boundary following the topography has a recharge zone and a discharge zone. The recharge zone stretches from the southern boundary to the head of the drainage at the bottom of the slope. This is set as a constant flux boundary. The discharge zone stretches along the drainage to the northern model boundary. This is conceptualized as a seepage face boundary. This means that if the water table reaches the model surface, all excess water flows out at the surface. If, during the simulation, the water table drops below the model surface, the surface is a

no-flow boundary. At the northern boundary, all remaining groundwater is assumed to discharge at the NE-SW drainage. Therefore, this boundary is also a no-flow boundary. Water enters the model on the elevated region to the south and flows north crossing the NFZ and discharging downslope south of the NFZ, flows downslope to the north, and discharges along the drainage.

Boundary fluxes can be highly variable due to spatial variations in precipitation and topographic and geologic influences on infiltration. Hillslopes and fine-grained rocks tend to decrease infiltration rates. As stated in section 2.3.3, average precipitation at the SSFL is ~18 in/yr (~0.004 ft/d), and infiltration rates are between <1% and 12% of precipitation. Therefore, the resulting flux range is $< 4 \times 10^{-5}$ ft/d to 0.00048 ft/d. Past studies have used an infiltration rate of 8% (AquaResource/MWH, 2007). For this simulation, the flux in the elevated region south of the NFZ is set to 0.0003 ft/d. The flux on the hillslope north of the NFZ is set to 0.0001 ft/d. Where the NFZ, ELV, and SPA intersect the surface, the flux is set to 1.6×10^{-5} ft/d.

3.4.3 Parameters of Interest

Parameters of interest are the hydraulic conductivity of the fault zone and the hydrostratigraphic units and the anisotropy of conductivity. Conductivity and anisotropy values were prescribed for each region of the model and were adjusted during the simulation runs while all other model parameters were held constant for all simulation runs.

Hydraulic conductivity can vary several orders of magnitude even within hydrostratigraphic units. Past hydraulic testing at the SSFL has produced estimates of hydraulic conductivity for various regions. For the Upper and Lower Burro Flats Members, the range is 10^{-6} - 10^{-5} cm/s (10^{-3} - 10^{-2} ft/d). For fine-grained units like the ELV and SPA Members, this range is $<10^{-6}$ cm/s (<0.003 ft/d) or about one order of magnitude below the sandstone units. These

ranges are used to guide the selection of starting estimates but are not considered end-point limits for calibration.

More freedom is allowed in calibrating the hydraulic conductivity of the NFZ. For scenarios in which the NFZ is considered a barrier to flow, the NFZ is represented as a uniform low conductivity zone. For scenarios in which the NFZ is considered a partial barrier to flow, the NFZ is represented as having a low conductivity upper zone and a moderate to high conductivity lower zone. The upper zone, where the NFZ crosscuts the Upper Burro Flats and ELV, is assigned a conductivity less than or equal to that of the low conductivity units. The lower zone, where the NFZ crosscuts the Lower Burro Flats, SPA, and Silvernale, is assigned a conductivity similar to that of adjacent sandstone units. In all scenarios, fault parallel anisotropy is imposed within the NFZ at a ratio of 10:1.

Anisotropy of conductivity is used to simulate the connectivity of the fracture network. Anisotropy is not uniquely characterized at the SSFL. However, it is well known that layered sedimentary systems generally have strong bedding parallel anisotropy. Anisotropy ratios in shales and siltstones are typically ~10:1 meaning that conductivity parallel to bedding is 10 times greater than conductivity normal to bedding. Anisotropy ratios in sandstones are typically higher because fine-grained interbeds tend to be frequent. These ratios range from 50:1 to 100:1 (AquaResource/MWH, 2007). These values are assigned to simulate the case of low fracture connectivity in which bedding parallel anisotropy dominates. For the case of strong fracture connectivity, an isotropic model is used.

3.4.4 Simulation Scenarios

The simulation runs were divided into two series. One series was run with an anisotropic model. These simulations considered a scenario in which the flow is largely controlled by bedding. Sandstone anisotropy was assumed to be 50:1, and fine-grained anisotropy was assumed to be

10:1. The other series was run with an isotropic model. These simulations considered a scenario in which the flow is largely controlled by a fracture network that is strongly connected in all directions. As stated earlier, a fault parallel anisotropy of 10:1 for the NFZ was assumed in all simulation runs. Both simulation series consisted of four simulations. The first was a simple, homogeneous scenario in which neither the NFZ nor fine-grained units existed. For the second, heterogeneity was increased by including the fine-grained ELV and SPA Members. For the third, the NFZ was added as a uniform, low-conductivity barrier. The fourth and final set of simulations considered scenarios in which the upper NFZ was a low-conductivity barrier, and the lower NFZ was much less of a barrier. Diagrams of the simulation scenarios are shown in Figure 3.6.

In each simulation run, the hydraulic conductivities of the model regions were adjusted until calculated heads matched field measured heads as closely as possible. To compare the modeled heads with the measured water level elevations, residuals were calculated at each observation point by subtracting the measured value from the simulated value. As a rule of thumb, acceptable residuals should be ~10% of the total range of measured water levels. This criterion was used for most of observation points. However, since head matching was not one of the objectives of this study, residuals up to 15% of the range were considered acceptable for some wells. For the ND-124 well-screens, a residual of 20% was accepted because the well is projected onto the model cross-section from a higher elevation off section.

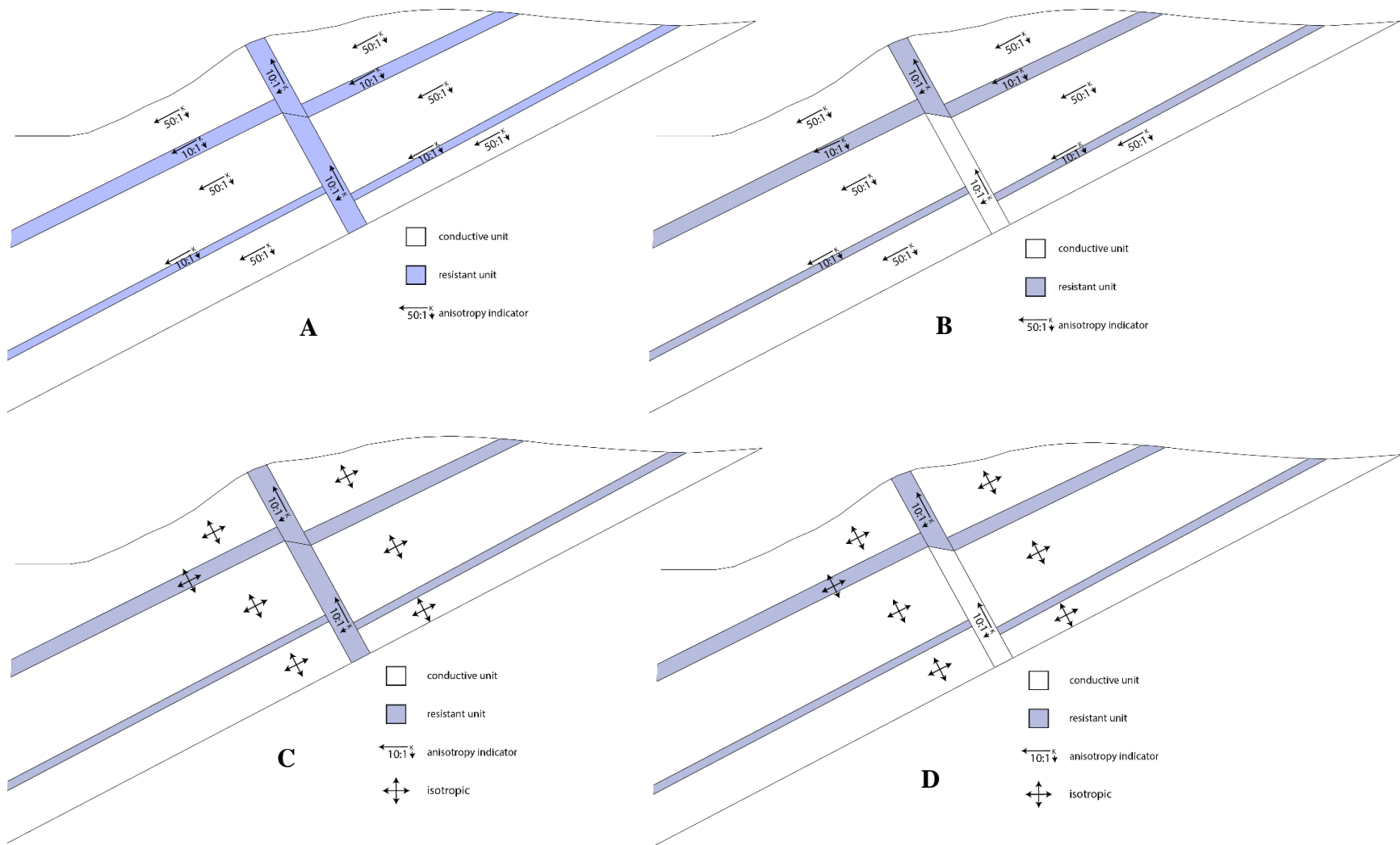


Figure 3.6 Diagrams of the simulation scenarios. (A) Anisotropic full barrier simulation; (B) Anisotropic partial barrier simulation; (C) Isotropic full barrier simulation; (D) Isotropic partial barrier simulation.

Chapter 4: Results and Discussion

4.1 Anisotropic Simulations

In this section, the results of the anisotropic simulation series are presented and discussed. The simulation results are shown in figures 4.1-4.6. Calibrated hydraulic conductivity values are given in Tables 4.1 and 4.2.

4.1.1 Scenarios without NFZ

The first anisotropic scenario simulates a homogeneous sandstone aquifer without the NFZ or fine-grained units. As shown in Figure 4.1, the head contours dip to the north. In the southern part of the model, flow lines are parallel to bedding, and upward flow does not occur until further to the north where the upward gradient increases. The transition from bedding parallel flow to upward flow is drastic and abrupt. The water table is a subdued expression of the topography without any abrupt changes. Calibration resulted in a hydraulic conductivity of 0.0125 ft/d. This calibration achieved low residuals in the southern observation points. However, without a sharp drop in the water table, head matching at observation points immediately north of the NFZ was not feasible. The strong vertical component to the head gradient further to the north made head matching at the northernmost observation points infeasible as well.

In the next anisotropic simulation, the fine-grained units were added as low conductivity units. As shown in Figure 4.2, the addition of these low conductivity features altered the flow regime very little. Head contours and flow lines are much the same as in the previous simulation. In a few instances where flow lines intersect low conductivity zones, the flow lines turn sharply upward through the low conductivity zone. No downward flow is observed across low conductivity zones. As in the homogeneous simulation, there are no sharp changes in water table elevation. To achieve reasonable heads, conductivity of the sandstone units was increased slightly to 0.013 ft/d and the conductivity of the fine-grained units was set to 0.0013 ft/d.

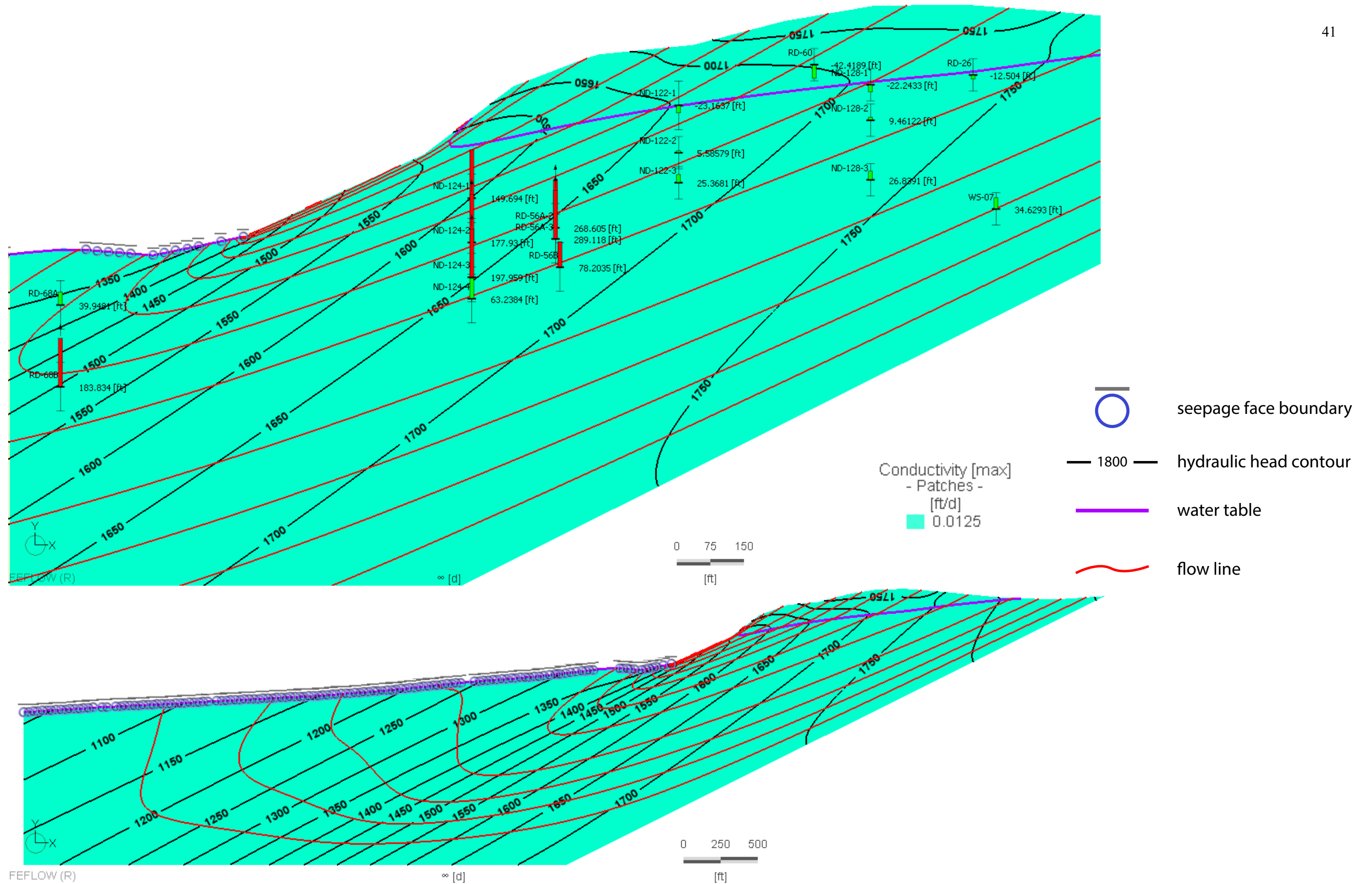


Figure 4.1 Results of the anisotropic simulation with homogeneous conductivity.

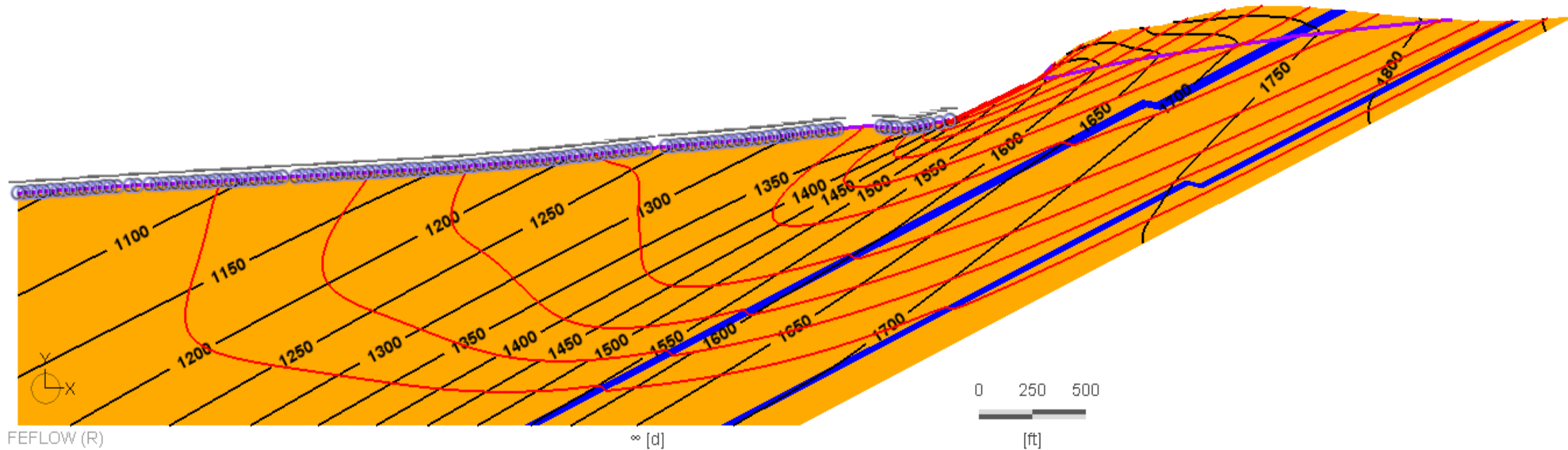
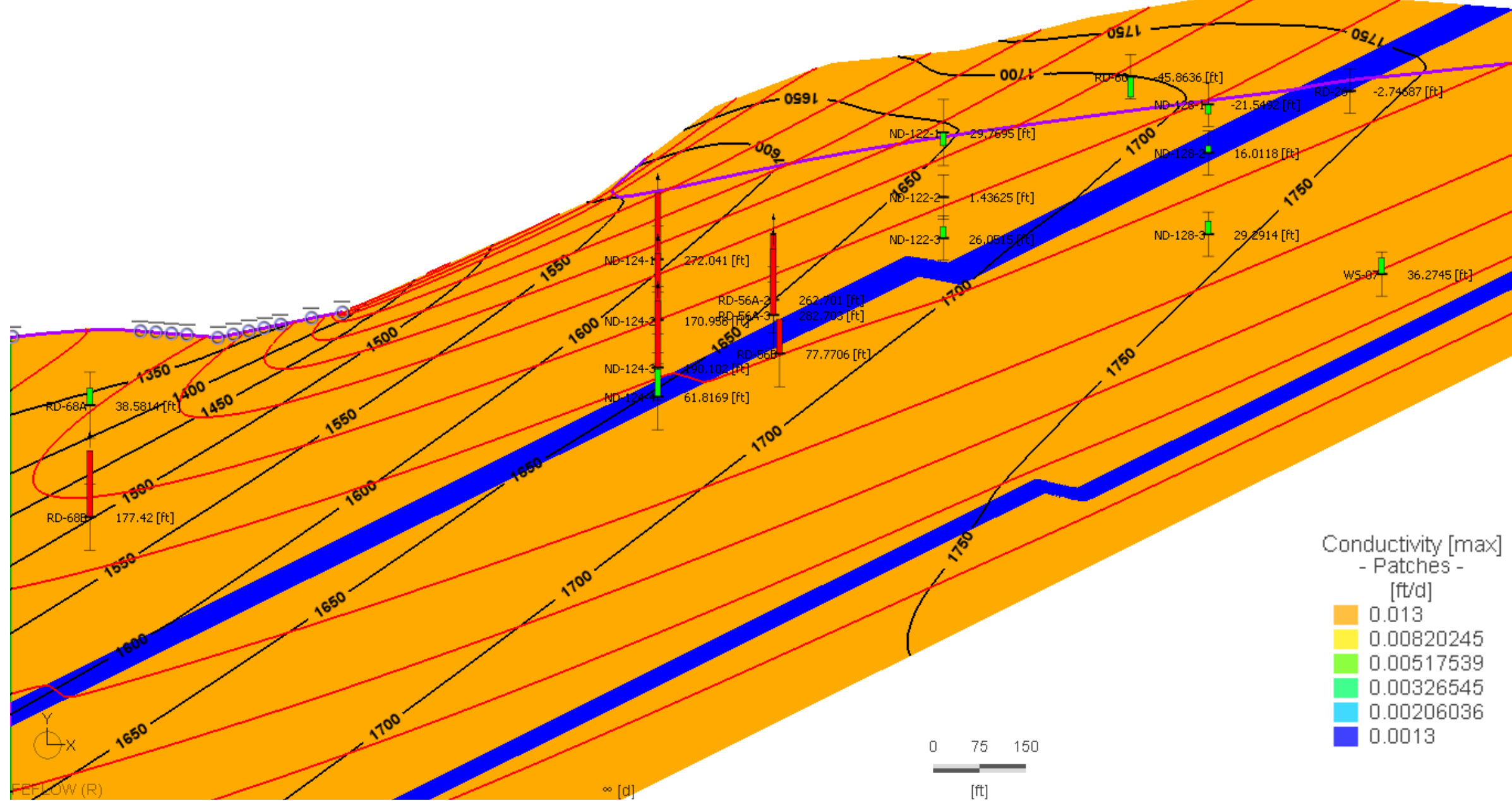


Figure 4.2 Results of the anisotropic simulation with fine-grained units and no NFZ.

4.1.2 Uniform Fault Barrier Scenario

In the next anisotropic simulation, the NFZ was added as a uniform low conductivity feature with conductivity similar to that of the fine-grained units and fault parallel anisotropy of 10:1. This simulates a scenario in which the NFZ acts as a uniform barrier to flow. The initial, uncalibrated simulation results are shown in Figure 4.3. The addition of the NFZ caused heads to greatly increase to the south creating a head drop of nearly 400 ft. The calibrated results are shown in Figure 4.4. Increasing the conductivity of the northern Upper Burro Flats brought heads down across the entire model domain. The conductivity of the NFZ was also increased to reduce the head drop to a more reasonable value. The conductivity differential between the southern and northern Upper Burro Flats is not entirely geologically unreasonable since turbidites are known to have significant lateral heterogeneities. This differential seems to cause the gradient north of the NFZ to be less pronounced than to the south. As a result, the magnitude of the head-drop decreases with depth. There is also a very large gradient across the northern ELV. Since the gradients throughout the model domain are more vertical than horizontal, the position of the water table is significantly higher than the heads calculated at the observation points. Upward flow is observed in the lower NFZ, and some upwelling occurs north of the NFZ.

Table 4.1 Calibrated hydraulic conductivity values for the anisotropic uniform fault barrier simulation

		Calibrated Hydraulic Conductivity at 26.5° angle (ft/d)
Shale 3/Simi/ Valley Fill		0.015
Upper Burro Flats	northern	0.06
	southern	0.013
ELV	northern	0.001
	southern	0.001
Lower Burro Flats	northern	0.01
	southern	0.013
SPA	northern	0.001
	southern	0.001
Silvernale	northern	0.013
	southern	0.013
NFZ	upper	0.003
	lower	0.003

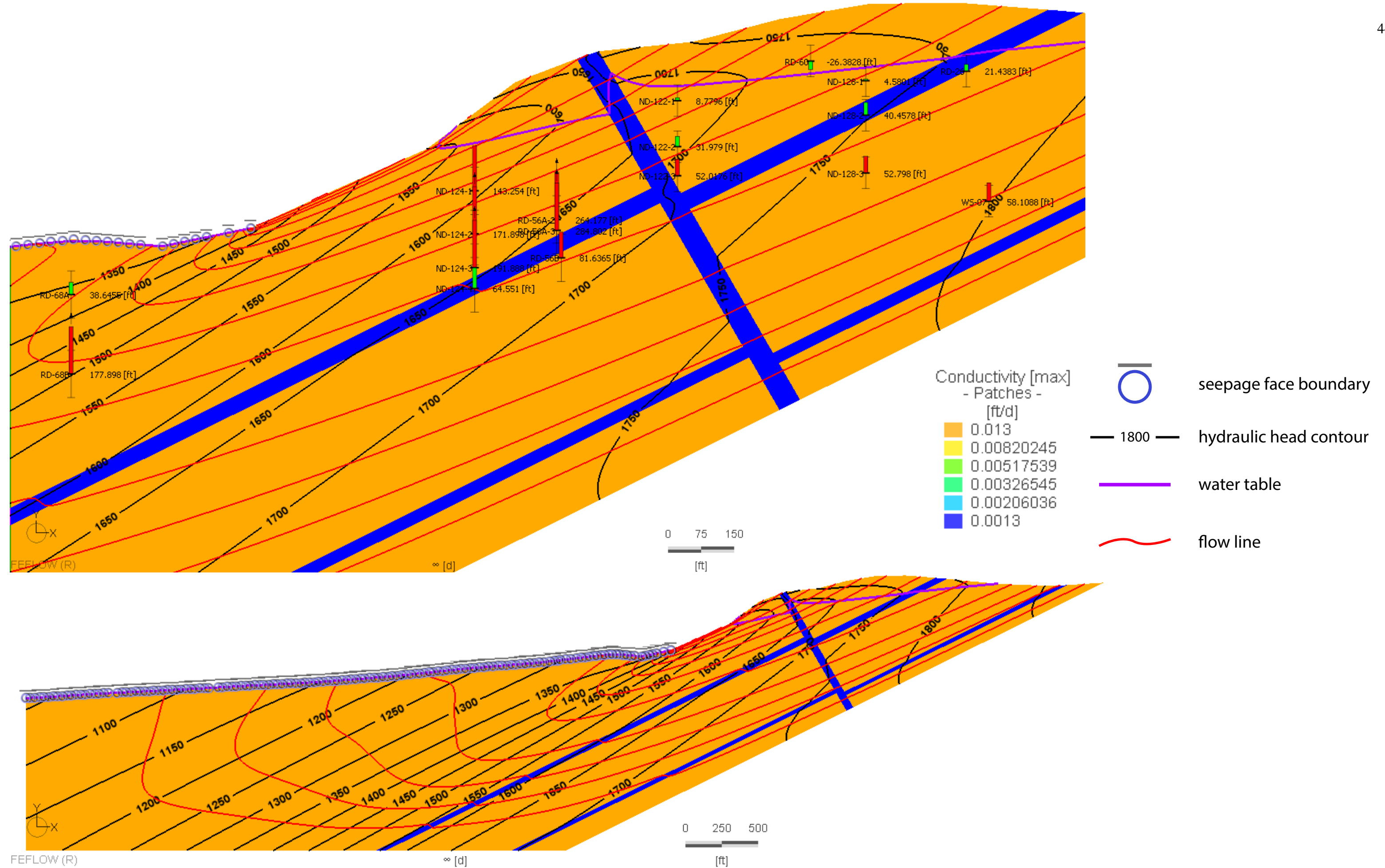
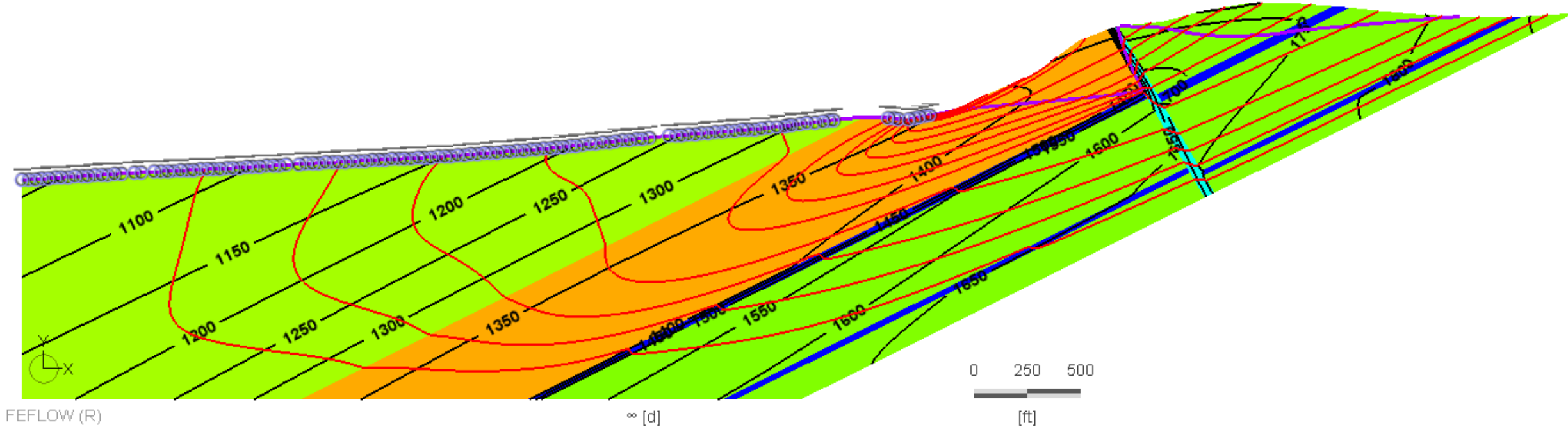
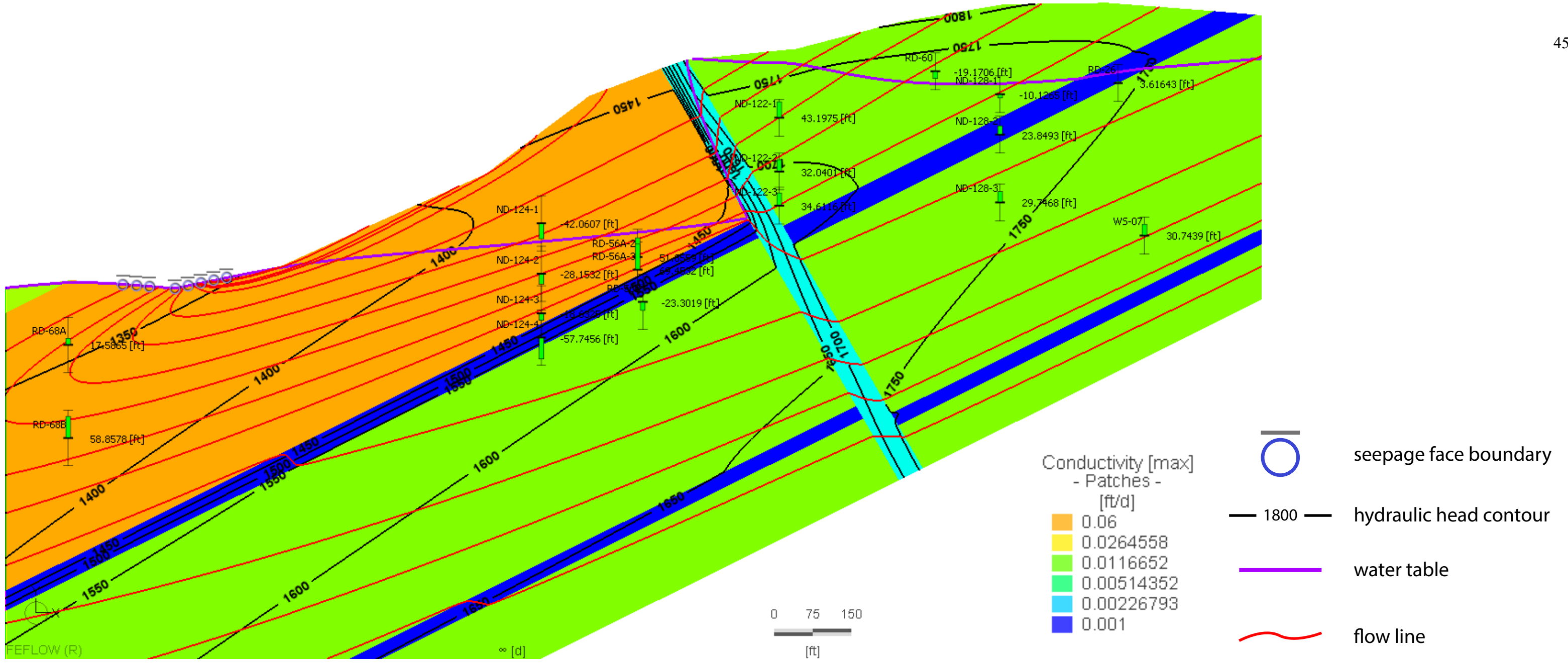


Figure 4.3 Results of the anisotropic simulation with the NFZ represented as a uniform low-conductivity barrier.



FEFLOW (R) [d] [ft]

Figure 4.4 Calibrated results of the anisotropic uniform low-K barrier simulation scenario.

4.1.3 Partial Fault Barrier Scenario

For the final anisotropic simulation, the NFZ was changed from a uniform barrier to a partial barrier with higher conductivity in the lower zone (below the ELV). The results of the initial simulation run for this scenario are shown in Figure 4.5. Head matches were generally good with the only exception being the observation point corresponding to the RD-26 well-screen. Minor conductivity adjustments were made to achieve slightly better residuals. These results are shown in Figure 4.6. Overall, increasing the conductivity of the lower NFZ did not significantly change the head distribution. However, upward flow within the NFZ increased as did upwelling on north of the NFZ.

Table 4.2 Calibrated hydraulic conductivity values for the anisotropic partial fault barrier simulation

		Calibrated Hydraulic Conductivity at 26.5° angle (ft/d)
Shale 3/Simi/ Valley Fill		0.013
Upper Burro Flats	northern	0.06
	southern	0.006
ELV	northern	0.001
	southern	0.001
Lower Burro Flats	northern	0.01
	southern	0.006
SPA	northern	0.001
	southern	0.001
Silvernale	northern	0.013
	southern	0.013
NFZ	upper	0.003
	lower	0.008

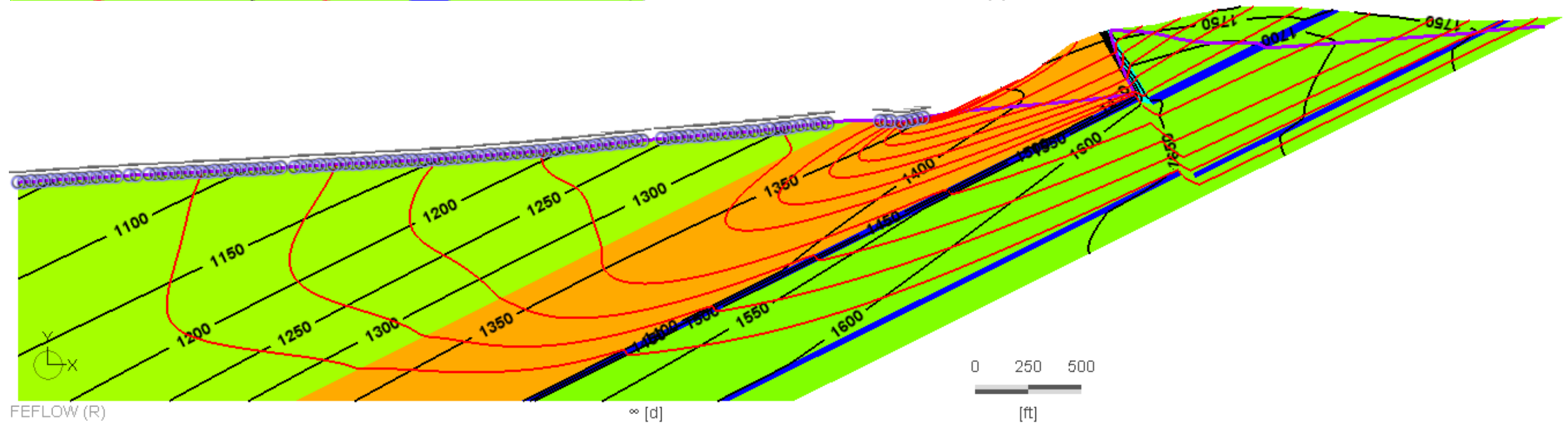
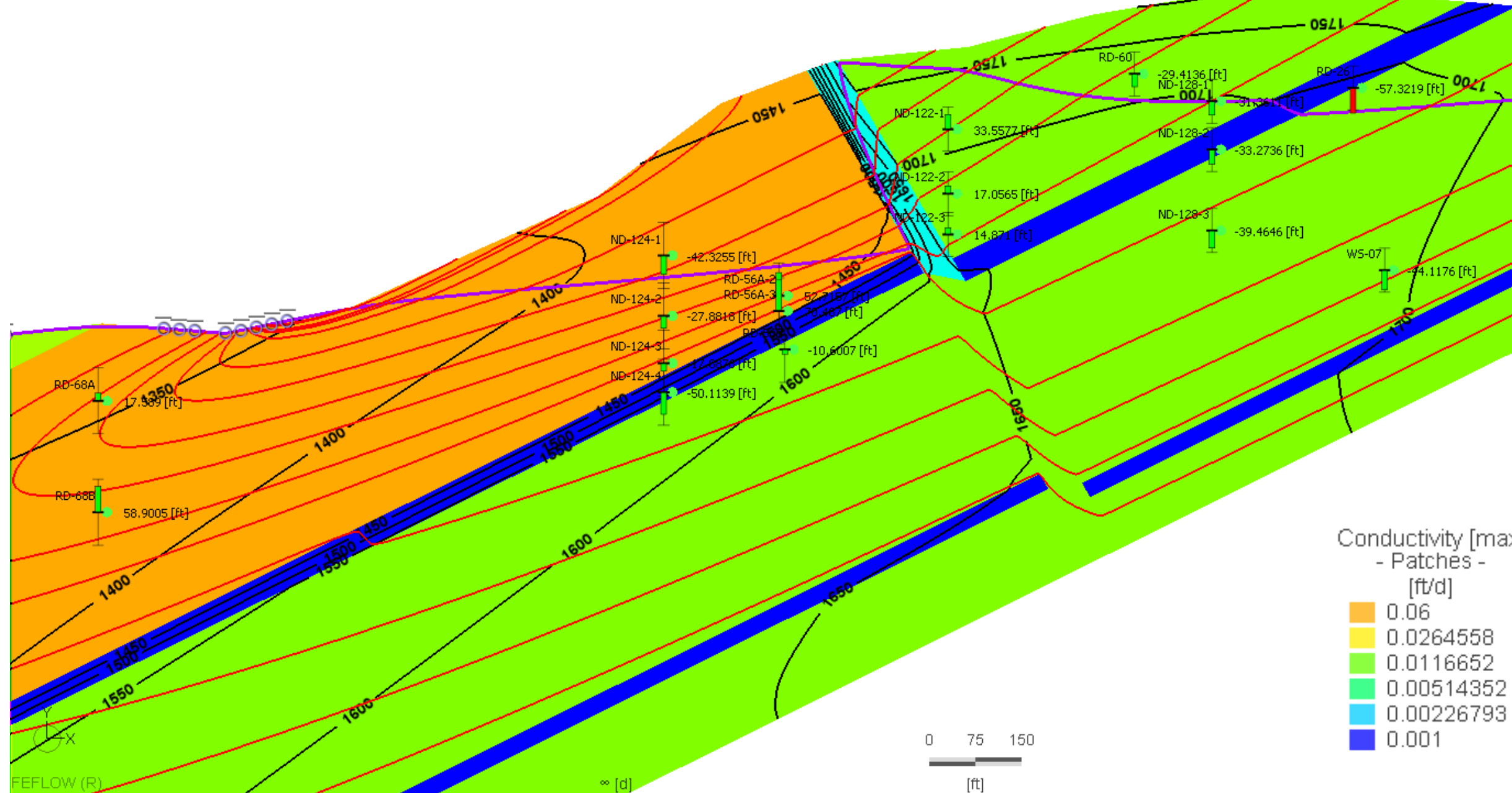


Figure 4.5 Initial results of the anisotropic simulation with the NFZ represented as a low-conductivity barrier above the ELV and as a more conductive zone below the ELV.

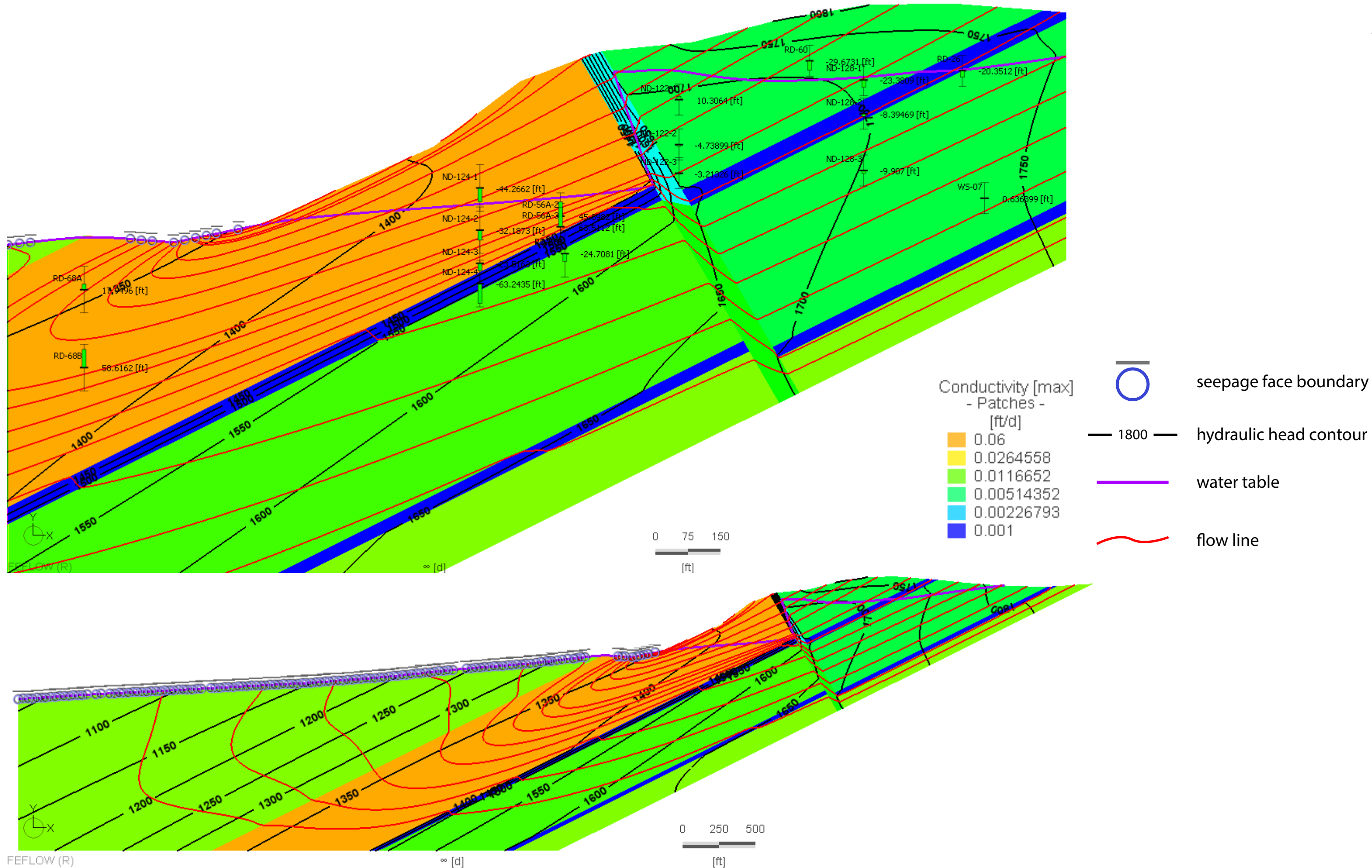


Figure 4.6 Calibrated results of the anisotropic partial barrier simulation scenario.

4.2 Isotropic Simulations

In this section, the results of the isotropic simulation series are presented and discussed. The progression of isotropic simulation scenarios is similar to that of the anisotropic simulations. The simulation results are shown in Figures 4.7-4.12. Calibrated hydraulic conductivity values are given in Tables 4.3 and 4.4.

4.2.1 Scenarios without NFZ

The first isotropic scenario simulates a homogeneous sandstone aquifer without the NFZ or fine-grained units. As shown in Figure 4.7, head contours are generally normal to bedding. Flow lines begin as parallel to bedding in the south and gradually bend upward to the north within the discharge zone. The water table is a subdued expression of the topography without any abrupt changes. The calibrated conductivity was 0.0035 ft/d, which is on the low end of the range of reasonable values for this sandstone. Heads are well matched at the southern observation points. without any head-drop, matching heads to the north was not feasible. However, very good head matches were obtained at the northernmost observation points.

In the next isotropic simulation, the fine-grained units were added as low conductivity units. As shown in Figure 4.8, the addition of these features did not significantly alter the flow regime. Minor deviations occur in flow lines across low conductivity units, but the overall flow directions remain the same. Minimal downward flow occurs across low conductivity zones. And no upwelling occurs until the discharge zone. No changes to the conductivity of the sandstone units were necessary. The conductivity of the fine-grained units was set to 0.00035 ft/d which is on the low end of the acceptable range, but still a reasonable value.

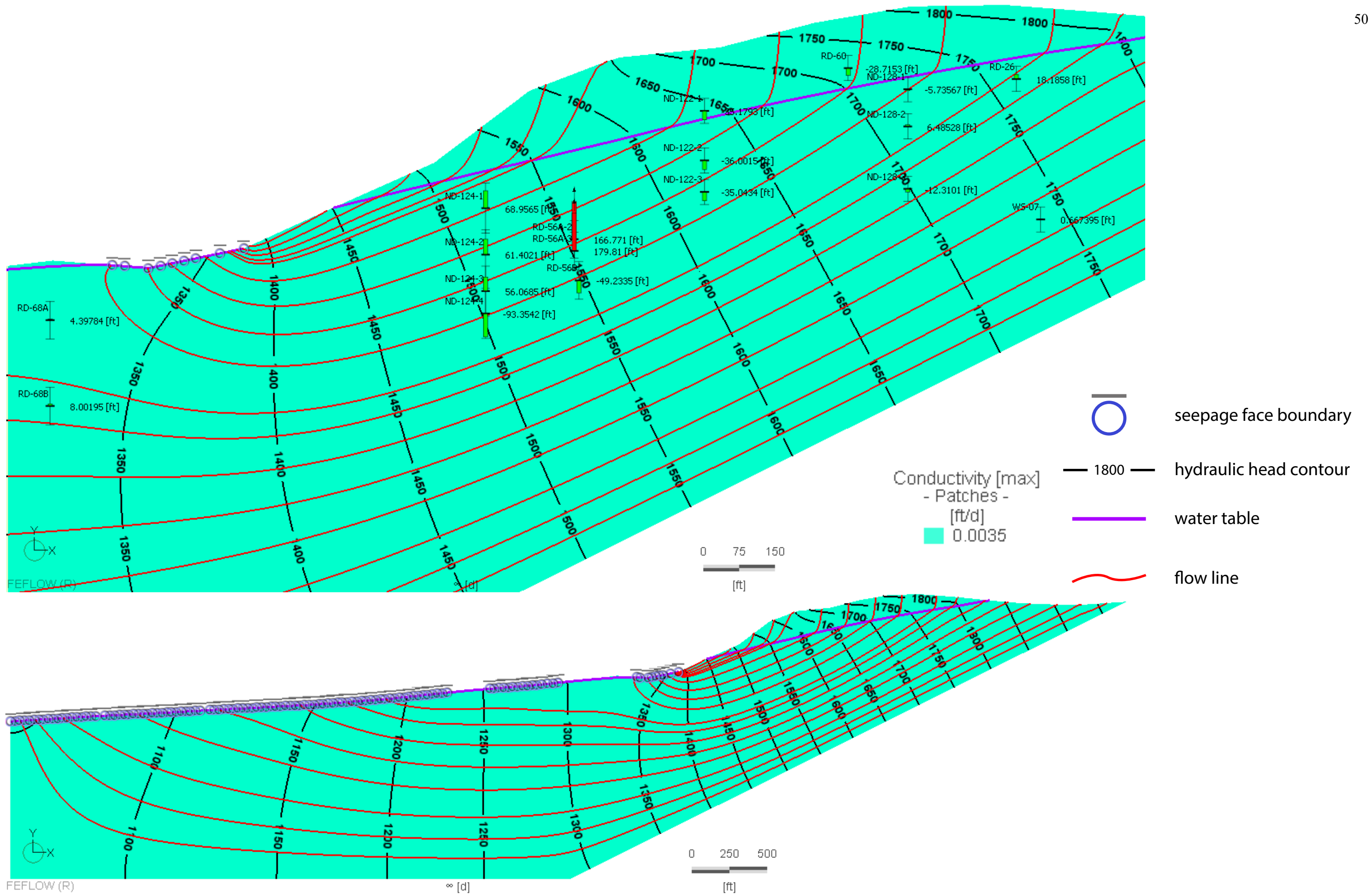


Figure 4.7 Results of the isotropic simulation with homogeneous conductivity.

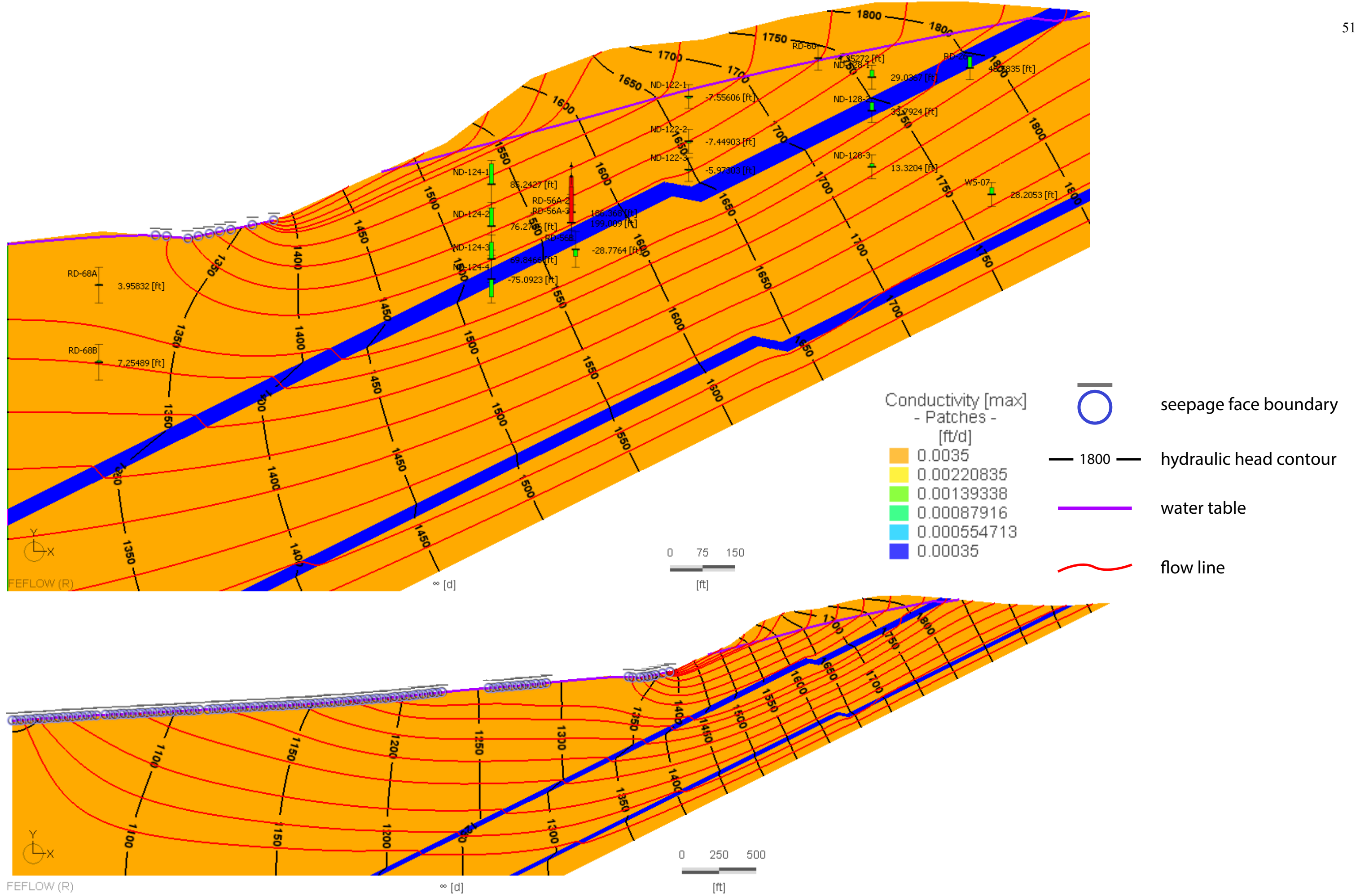


Figure 4.8 Results of the anisotropic simulation with fine-grained units included and NFZ excluded.

4.2.2 Uniform Fault Barrier Scenario

For the next isotropic simulation, the NFZ was added as a uniform low-conductivity feature with conductivity similar to that of the fine-grained units and fault parallel anisotropy of 10:1. The initial, uncalibrated simulation results are shown in Figure 4.9. The addition of the fault as a uniform barrier caused substantial increases in heads to the south, whereas heads to the north remained mostly unchanged. The results of the calibrated simulation run are shown in Figure 4.10. In order to lower heads across the board, the conductivity of the sandstone and fine-grained units was increased to 0.01 ft/d and 0.001 ft/d respectively. The conductivity of the NFZ was increased slightly to 0.0017 to further decrease the heads in the south. Head matches were not achieved at observation points in the northern Lower Burro Flats. Because of the isotropy, the head-drop within the Upper Burro Flats was the same as the head-drop in the Lower Burro Flats. Therefore, head matching in the northern Lower Burro Flats could not be achieved without decreasing the conductivity of that region to an unreasonably low value which would, in turn, drive up heads to the south. Since the overall head gradient is mostly horizontal, the position of the water table is closely linked to heads at observation points. Significant vertical flow occurs south of the NFZ, but minimal upwelling occurs north of the NFZ.

Table 4.3 Calibrated hydraulic conductivity values for the isotropic uniform fault barrier simulation

		Calibrated Isotropic Hydraulic Conductivity (ft/d)
Shale 3/Simi/ Valley Fill		0.01
Upper Burro Flats	northern	0.01
	southern	0.01
ELV	northern	0.0008
	southern	0.001
Lower Burro Flats	northern	0.01
	southern	0.01
SPA	northern	0.001
	southern	0.001
Silvernale	northern	0.01
	southern	0.01
NFZ	upper	0.0017
	lower	0.0017

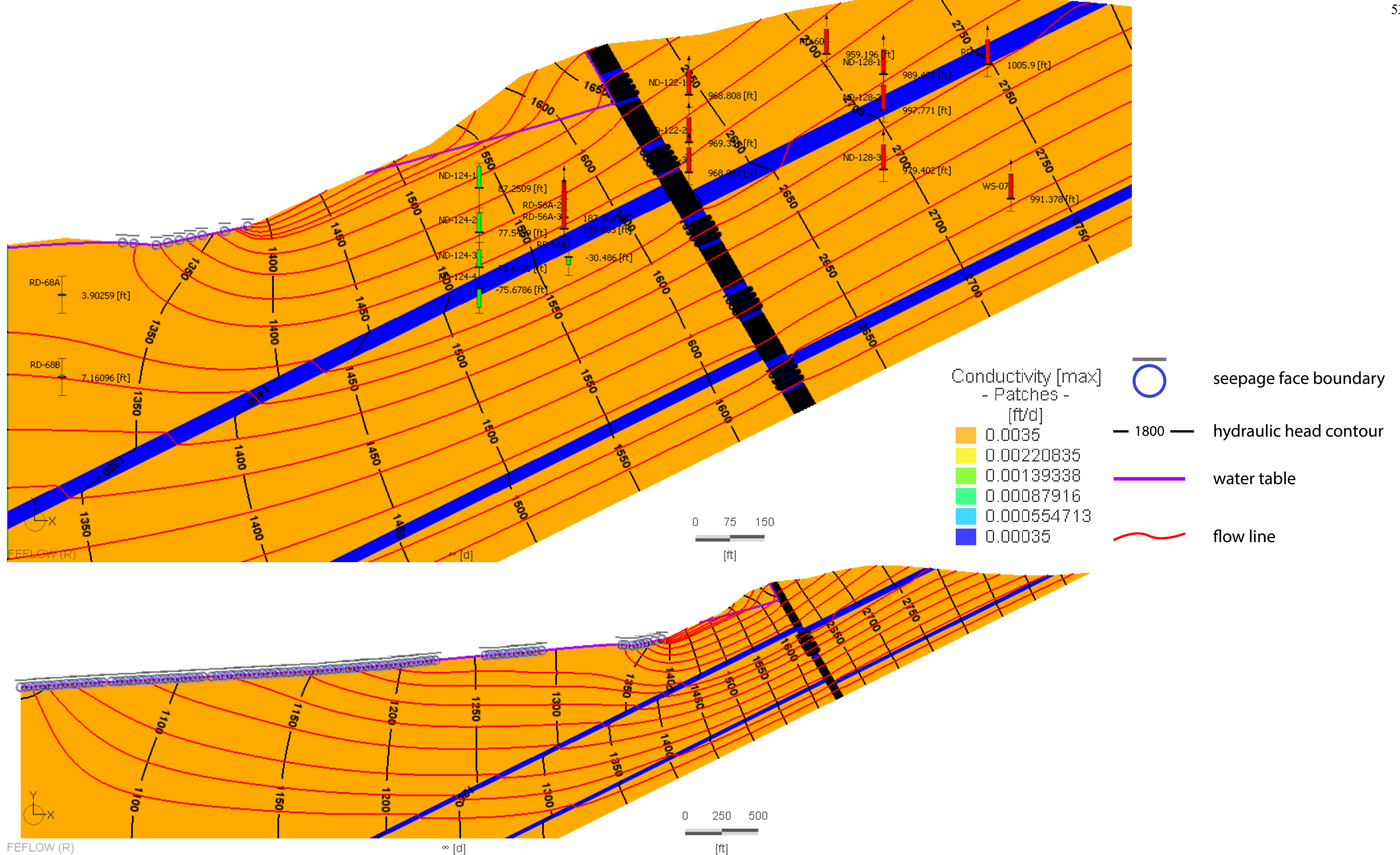


Figure 4.9 Initial results of the isotropic simulation with the NFZ represented as a uniform low-conductivity barrier.

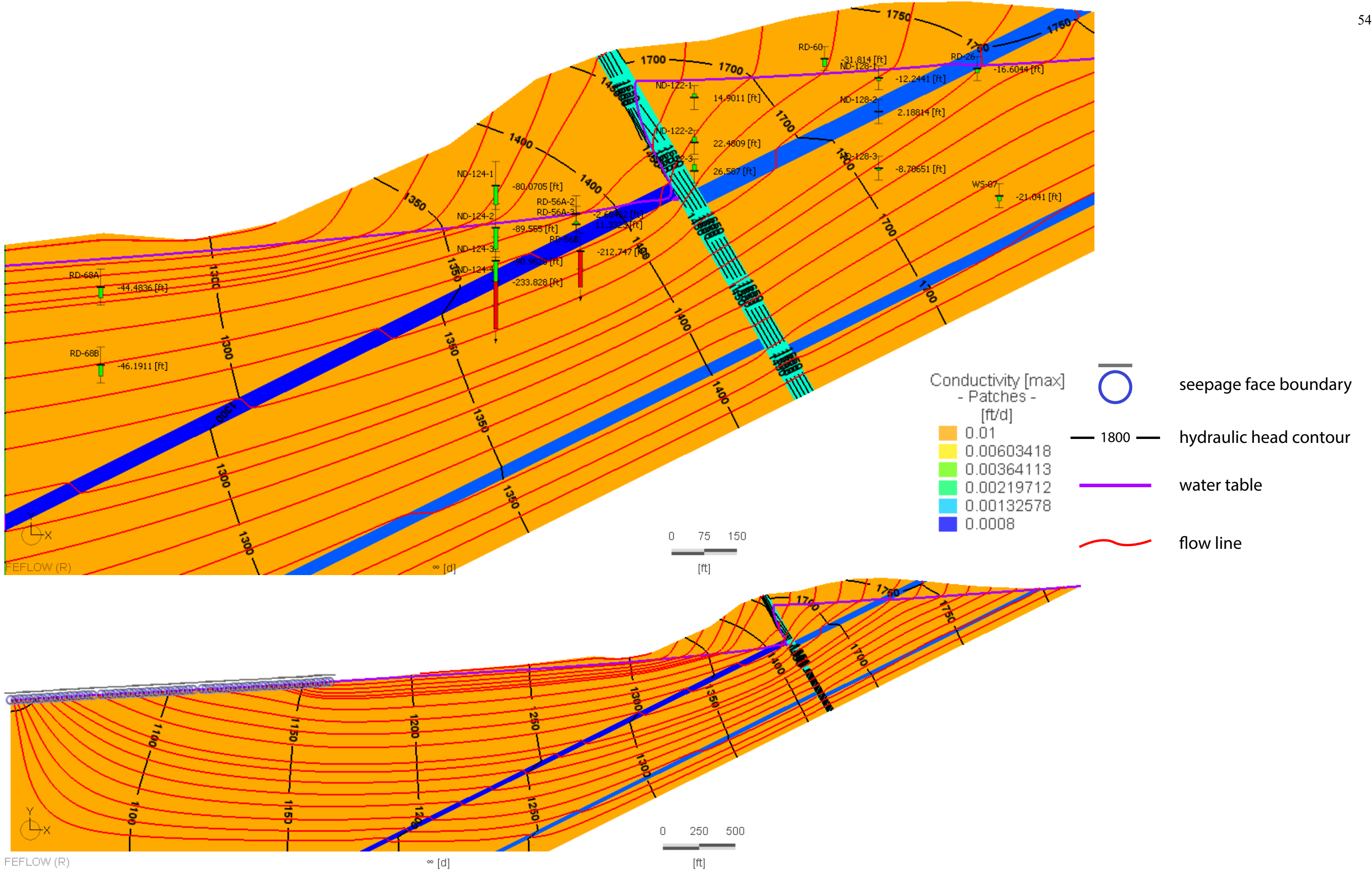


Figure 4.10 Calibrated results of the isotropic uniform barrier simulation scenario.

4.2.3 Partial Fault Barrier Scenario

For the final isotropic simulation, the NFZ was changed from a uniform barrier to a partial barrier with higher conductivity in the lower zone (below the ELV). Initially, as shown in Figure 4.11, the increase of conductivity in the lower NFZ greatly reduced the heads to the south which, consequently, greatly reduced the magnitude of the head-drop. Significant adjustment of the conductivity zones was necessary to achieve an acceptable calibration. The results of the calibrated simulation are shown in Figure 4.12. Conductivity of the Lower Burro Flats was greatly reduced but was still within the range of acceptable values. Additionally, the conductivity of the northern ELV was reduced to two orders of magnitude lower than that of the southern ELV in order to further raise heads in the northern Lower Burro Flats. A decrease in conductivity of the upper NFZ was necessary to increase the head-drop. Vertical downward flow in the south increased, as did upwelling to the north.

Table 4.4 Calibrated hydraulic conductivity values for the isotropic partial fault barrier simulation

		Calibrated Isotropic Hydraulic Conductivity (ft/d)
Shale 3/Simi/ Valley Fill		0.01
Upper Burro Flats	northern	0.01
	southern	0.01
ELV	northern	0.00008
	southern	0.001
Lower Burro Flats	northern	0.003
	southern	0.005
SPA	northern	0.001
	southern	0.001
Silvernale	northern	0.01
	southern	0.01
NFZ	upper	0.0008
	lower	0.01

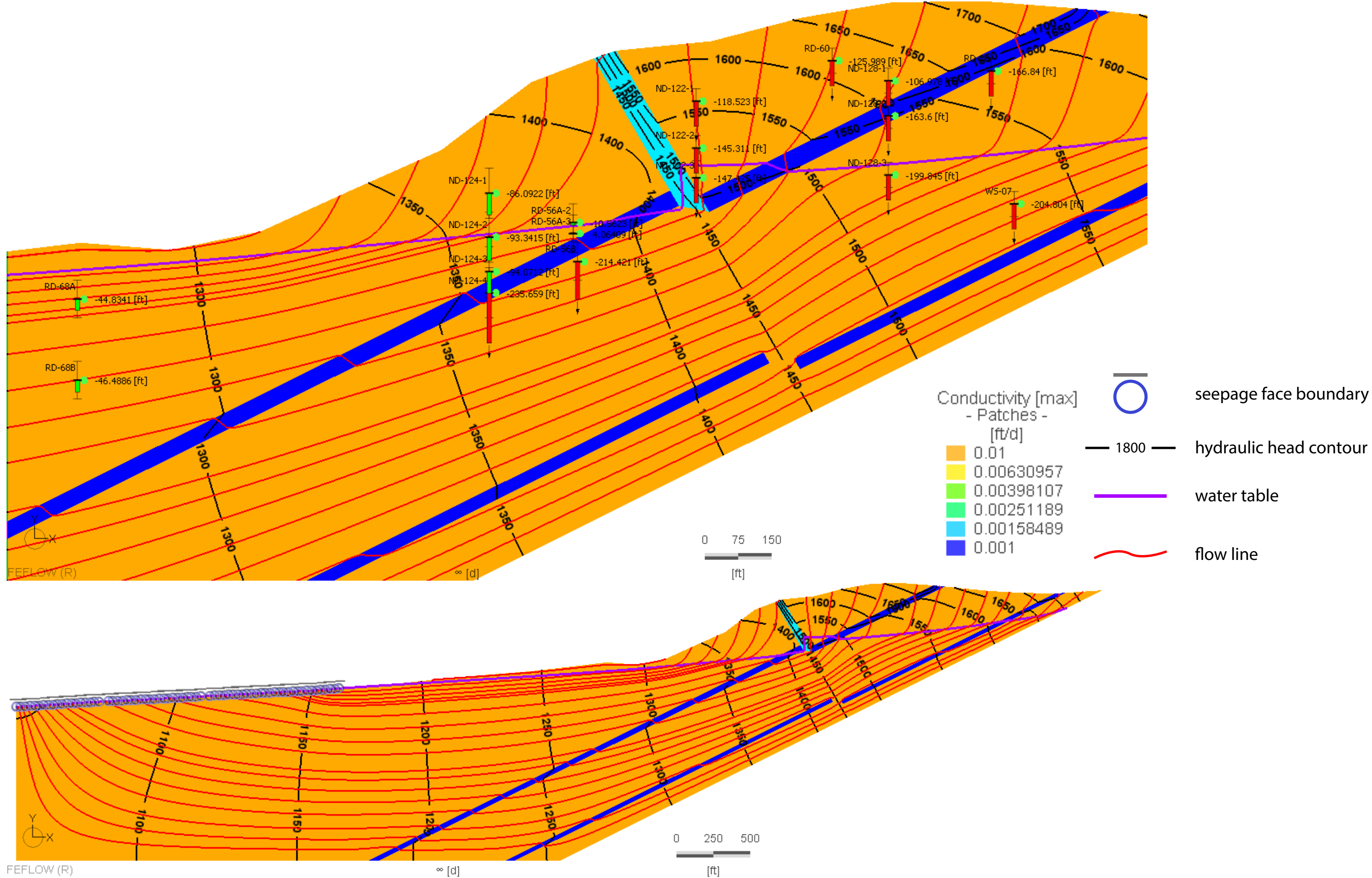


Figure 4.11 Initial results of the isotropic simulation with the NFZ represented as a low-K barrier above the ELV and a more conductive zone below.

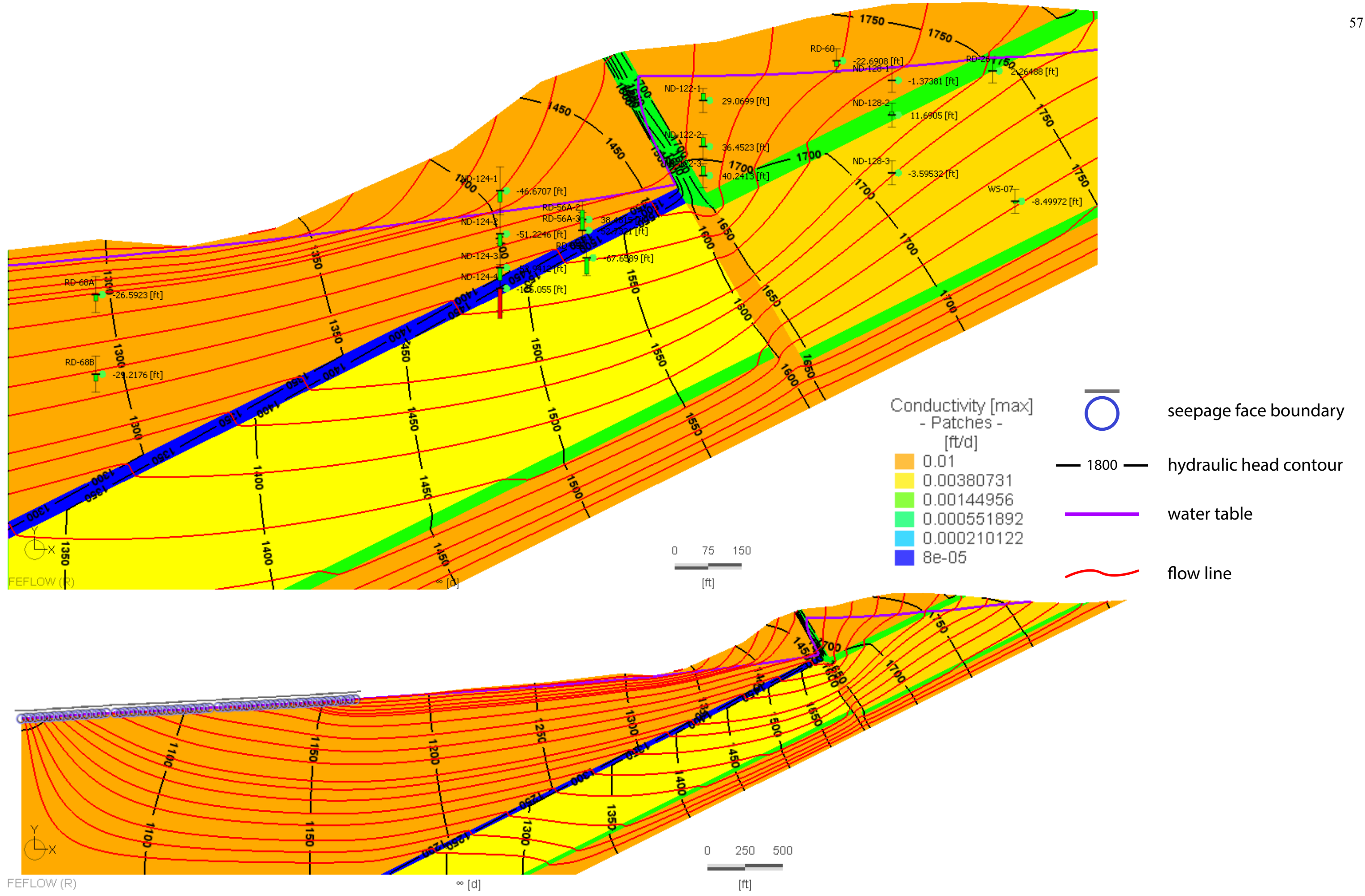


Figure 4.12 Calibrated results of the isotropic partial barrier simulation scenario.

4.3 Discussion

In this section, we compare the anisotropic and isotropic simulation series and discuss what can be inferred about the validity of the various elements of the conceptual model outlined in section 3.2. Primarily, the goal is to deliberate between the bedding control and fracture control hypotheses and between the uniform fault barrier and partial fault barrier hypotheses. These findings are discussed in relation to other studies and observations at the SSFL. We also discuss implications for other studies. A summary matrix of the simulation results is provided in Table 4.5.

4.3.1 Simulation Comparisons

First, we consider the simulations from each series that were done without the NFZ. The main difference between the anisotropic and isotropic simulations was the orientation of the hydraulic head contours. In the anisotropic simulations, head contours are more horizontal which creates a more vertical hydraulic gradient. This gradient seems to be a result of increasing pressurization with depth due to frequent fine-grained interbedding within the sandstone. In the isotropic simulations, head contours are more vertical. The match between simulated and observed heads from both series was of similar quality; good head matches were achieved at southern observation points. However, the calibration of the isotropic simulations resulted in conductivities on the low end of the acceptable spectrum. Ultimately, these results do not provide evidence in support of either bedding-control or fracture-control. Since the NFZ was not present in these simulations, nothing can be said yet about the nature of the NFZ. However, the fact that the head-drop is absent supports the hypothesis that the NFZ is the cause of the head-drop.

The initial implementation of the NFZ had a much greater effect on heads in the isotropic scenario than in the anisotropic scenario. Therefore, conductivities in the isotropic scenario needed to be increased bringing them into the more central part of the acceptable spectrum. This

suggests that, if fracture connectivity is strong (isotropic scenario), the heads distribution is a result of the NFZ piling up heads to the south and that in the absence of the NFZ, heads would be much lower. In the anisotropic scenario, conductivity in the northern Upper Burro Flats needed to be significantly increased to achieve the observed head-drop. This suggests that in the anisotropic scenario, the offset in the water table, although still partly a result of the NFZ piling up heads to the south, the magnitude of the offset is more related to the change in conductivity between the southern and northern Upper Burro Flats Member. Such a drastic change could result from a facies change within the Upper Burro Flats, or it could be related to a higher degree of bedding-parallel fracturing. None of the data collected suggests that the Upper Burro Flats is more fractured north of the NFZ than to the south. Therefore, a facies change may be a more reasonable explanation.

In the partial barrier simulations, the increase in conductivity of the lower NFZ had a much greater effect on the isotropic simulation than the anisotropic simulation. This observation was expected considering the effects of initial implementation of the NFZ in both scenarios. For the anisotropic simulation, it did not seem to matter whether the NFZ was a uniform barrier or a partial barrier. In the isotropic scenario, the conductivity of the northern ELV needed to be significantly reduced to create the strong upward gradient north of the NFZ. This could be explained by a facies change within the ELV, but a reduction of two orders of magnitude over such a short distance seems unlikely.

In all simulation scenarios, flow in the Lower Burro Flats is strongly bedding parallel to the immediate north and south of the NFZ. However, in the anisotropic scenario, head-loss along flow lines is much less than in the isotropic scenario. Consequently, even though a low-conductivity lower NFZ causes some head loss, acceptable head matches could still be obtained without resulting to extreme conductivity values. Therefore, modeling results suggest that, in the anisotropic case, both the uniform and the partial fault barrier hypotheses should be considered

for further investigation. In the isotropic scenario, head-loss along flow lines is much greater, and the additional head-loss caused by the low-conductivity lower NFZ resulted in too much head-loss along flow lines for successful head matching to occur. Therefore, a more conductive lower NFZ was necessary for successful head matching. This suggests that, in the isotropic case, only the partial fault barrier hypothesis should be accepted.

4.3.2 Comparison with Other Observations

The discussion of modeling results revealed that at least one scenario from both simulation series has had a successful calibration. Therefore, modeling alone has not provided sufficient evidence for the bedding control hypothesis or the fracture control hypothesis. Therefore, we also consider the shape of the B204 COC plume (Figure 2.13). The downward flow south of the NFZ in the isotropic partial barrier scenario would facilitate the downward migration of COCs that appears to have occurred. This vertical flow is not seen in the anisotropic simulations. However, COCs at this site are dense non-aqueous phase liquids (DNAPLs). Therefore, it is possible that the initial downward migration was due to gravity driven density flow. The presence of COCs at the ND-128-4 well-screen suggest that vertical migration went at least as far down as the depth of that well screen before going into solution and being carried north by the flow of groundwater. COCs were found at RD-56A but not at RD-56B which suggests that upwelling into the Upper Burro Flats occurs north of the NFZ but south of RD-56B. In the isotropic partial barrier simulation, flow lines at the depth of ND-128-4 do not cross the ELV until much further north. This suggests that the isotropic scenario may not be the scenario that best fits the data and that in this part of the SSFL fracture connectivity is not a strong control. In the anisotropic simulations, upward flow within the NFZ causes deeper groundwater to upwell further south but still north of the NFZ. This is particularly evident in the partial barrier

simulation. However, to ultimately confirm the partial fault barrier hypothesis, rock samples from the NFZ should be analyzed for.

The suggestion that fracture connectivity is low in this portion of the SSFL is at odds with the findings cited earlier in this thesis from Cilona et al. (2016) who concluded that fracture connectivity was high in all directions. However, the Cilona et al. (2016) study looked at the SSFL as a whole. Therefore, a local departure from that conclusion is reasonable. Furthermore, CH2M Hill noted in a recent report for NASA (2017) that zones of increased fracturing did not necessarily correlate to increased conductivity. These findings further support the conclusion that, at least in this part of the SSFL, vertical fracture connectivity is not as important as the influence of bedding orientation on the flow regime.

Table 4.5 Matrix summarizing results of the four main simulation scenarios

	Uniform Barrier	Partial Barrier
Anisotropic	Conductivity of northern Upper Burro Flats increased Head loss across NFZ varies with depth along NFZ Flow across lower NFZ sufficient to maintain head in Lower Burro Flats Some upwelling across ELV immediately north of NFZ Considered viable scenario based on residuals	K of northern Upper Burro Flats increased Increased upwelling across ELV immediately north of NFZ Flow across lower NFZ sufficient to maintain head in Lower Burro Flats Considered viable scenario based on residuals
Isotropic	Head loss across NFZ is large and uniform with depth Flow across NFZ in Lower Burro Flats not sufficient to maintain head No upwelling across ELV to the north Not a viable scenario	Additional flow across lower NFZ Conductivity of northern ELV significantly reduced compared to south Vertical flow south of NFZ in Upper Burro Flats No upwelling across ELV until further to the north Considered a viable scenario based on residuals

4.3.3 Implications

Past modeling attempts have simulated the NFZ as having a conductivity similar to that of the sandstone units (AquaResource/MWH, 2007). Based on these results, the NFZ in this part of the SSFL should be represented as a low conductivity zone at least above the ELV. Past modeling attempts have also incorporated bedding parallel anisotropy into the models. These results do not completely validate this approach, but they do provide some evidence in support of it. These results also show that contaminants have migrated upward north of the NFZ as a result of

groundwater flow. Since transport predictions were not a part of this study, the results do not have implications for the future migration of COC plumes.

Chapter 5: Conclusions and Recommendations

5.1 Conclusions

The objective of this study was to investigate, through iterative modeling, the controls on the flow system at the B204 area, and the causes of the head-drop across the NFZ and why it is confined to the Upper Burro Flats.

Several controls on the flow regime were observed, however the relative importance of some of them was not evident. The most important control is topography. This determines the overall flow direction. Water flows in at topographic highs and flows out at topographic lows. Another observed control was the NFZ. The presence of the head-drop requires that the NFZ act as at least a partial barrier to flow. Other controls on the flow system are the orientation of the bedding and the connectivity of the fracture network. Ultimately the results of these simulations did not provide strong evidence that one of these was significantly more important than the other. However, when considered together with other studies and the shape of the COC plume, most of the results presented in this thesis seem to point toward bedding orientation as being the more dominant control.

What can be said with greater certainty is that if the fracture network is well connected vertically and horizontally, as suggested by Cilona (2016), the NFZ must be more permeable at depth than at its shallow reaches to sustain heads below the ELV. However, the shape of the COC plume points to a bedding controlled system. Modeling results suggest that both the anisotropic uniform barrier scenario and the anisotropic partial barrier scenario represent viable hypotheses. Therefore, if the bedding control hypothesis is accepted, more testing will be necessary to determine which NFZ hypothesis should be accepted.

5.2 Recommendations

The next step for this study would be to use an automatic parameter estimation program to calibrate the model. The manual calibration that was done for this study was valuable for understanding the large-scale processes at play. However, time limitations required the selection of a limited number of scenarios for calibration. A parameter estimation program would be able to run hundreds to thousands of scenarios within a short time period which would allow calibration of many more parameters than what was done for this study. Another recommendation for a future study is to obtain rock core samples of the NFZ at different depths and use observations and laboratory tests to inform the model. It would also be interesting to do a similar study to this one at another well transect along the NFZ to see if similar results are obtained elsewhere along strike of the fault zone. Additionally, although the two-dimensional approach used in this study proved to be effective at representing the most important features of the flow system, more in-depth models should be expanded to a three-dimensions. Furthermore, simulation of transient conditions would best be done with a double-porosity model.

References

- Antonellini, M., and Aydin, A. (1994). Effect of Faulting on Fluid Flow in Porous Sandstones: Petrophysical Properties. *AAPG Bull.* 78, 355–377.
- AquaResource, Inc., and MWH Americas, Inc. (2007). Three Dimensional Groundwater Flow Model Report, Santa Susana Field Laboratory, Ventura County, CA.
- Atwater, T.M. (1998). Plate Tectonic History of Southern California with emphasis on the Western Transverse Ranges and Northern Channel Islands. In *Contributions to the Geology of the Northern Channel Islands, Southern California*, P.W. Weigand, ed. (American Association of Petroleum Geologists, Pacific Section, MP 45), pp. 1–8.
- Bense, V.F., and Van Balen, R. (2004). The effect of fault relay and clay smearing on groundwater flow patterns in the Lower Rhine Embayment. *Basin Res.* 16, 397–411.
- Bense, V.F., Gleeson, T., Loveless, S.E., Bour, O., and Scibek, J. (2013). Fault Zone Hydrogeology. *Earth-Sci. Rev.* 127, 171–192.
- Cilona, A., Aydin, A., and Johnson, N.M. (2014). Permeability of a fault Zone crosscutting a sequence of sandstones and shales and its influence on hydraulic head distribution in the Chatsworth Formation, California, USA. *Hydrogeology Journal*. . . 10.1007/s10040-014-1206-1.
- Cilona, A., Aydin, A., Likerman, J., Parker, B., and Cherry, J. (2016). Structural and Statistical Characterization of Joints and Multi-scale Faults in an Alternating Sandstone and Shale Turbidite Sequence at the Santa Susana Field Laboratory: Implications for their Effects on Groundwater Flow and Contaminant Transport. *J. Struct. Geol.* 86, 95–114.
- Davatzes, N.C., and Aydin, A. (2005). Distribution and Nature of Fault Architecture in a Layered Sandstone and Shale Sequence: An Example from the Moab Fault, Utah. In *Faults, Fluid Flow and Petroleum Traps*, R. Sorkhabi, and Y. Tsuji, eds. pp. 153–180.
- Dibblee, T. W., 1992. Geologic Quadrangle Maps: Los Angeles and Ventura Counties, California. Dibblee Foundation Geologic Maps. (a) Moorpark Quadrangle; (b) Simi Quadrangle; (c) Santa Susana Quadrangle; (d) Oat Mountain Quadrangle; (e) Camarillo and Newbury Park Quadrangles; (f) Thousand Oaks Quadrangle; (g) Calabasas Quadrangle; (h) Canoga Park Quadrangle; (i) Point Mugu and Triunfo Pass Quadrangles; (j) Point Dume Quadrangle; (k) Malibu Beach Quadrangle; (l) Topanga Quadrangle
- Dierchsh, H.-J.G. (2014). *FEFLOW: Finite Element Modeling of Flow, Mass and Heat Transport in Porous and Fractured Media* (Springer).
- Environmental Protection Agency (2016). Trichloroethylene Fact Sheet.
- Haneberg, W.C. (1995). Steady state groundwater flow across idealized faults. *Water Resour. Res.* 31, 1815–1820.

Jourde, H., Flodin, E.A., Aydin, A., Durlofsky, L.J., and Wen, X.-H. (2002). Computing permeability of fault zones in eolian sandstone from outcrop measurements. *AAPG Bull.* 86, 1187–1200.

Link, M. H., Squires, R. L, Colburn, I. P., 1981. Simi Hills Cretaceous Turbidites, Southern California, Field Trip Guidebook, Pacific Section of the Society of Economic Paleontologists and Mineralogists.

Medeiros, W.E., do Nascimento, A.F., Alves de Silva, F.C., Destro, N., and Demétrio, J.G.A. (2010). Evidence of hydraulic connectivity across deformation bands from field pumping tests: Two examples from Tucano Basin, NE Brazil. *J. Struct. Geol.* 32, 1783–1791.

MWH Americas, Inc. (2007). Geologic Characterization of the Central Santa Susana Field Laboratory Ventura County, CA.

MWH Americas, Inc. (2009). Draft Site-Wide Remedial Investigation Report Santa Susana Field Laboratory.

National Aeronautics and Space Administration (NASA) (2017). B204/ELV AIG Data Evaluation Report, Santa Susana Field Laboratory, Ventura County, California.

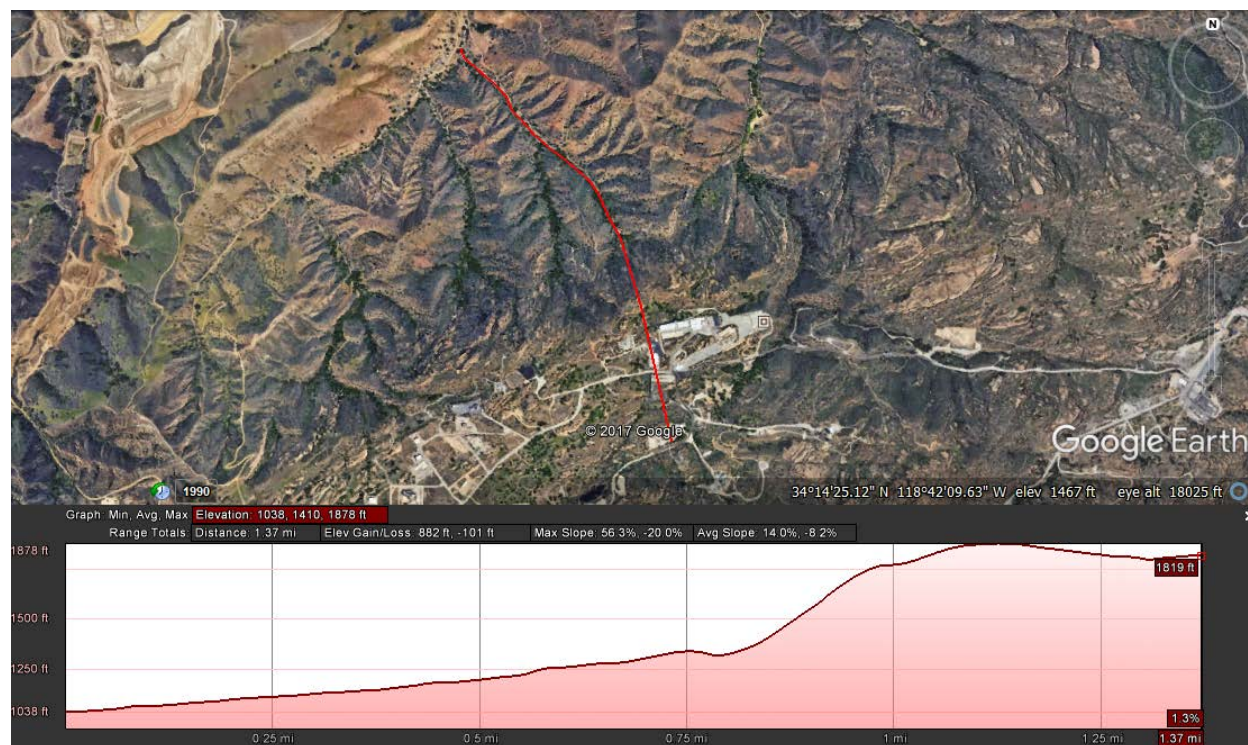
Office of Inspector General (2014). NASA's Environmental Remediation Efforts at Santa Susana Field Laboratory.

Appendix A: Mesh Development

Building the finite element was done in three steps: (1) create a surface profile; (2) build a two-dimensional supermesh; and (3) generate the finite element mesh.

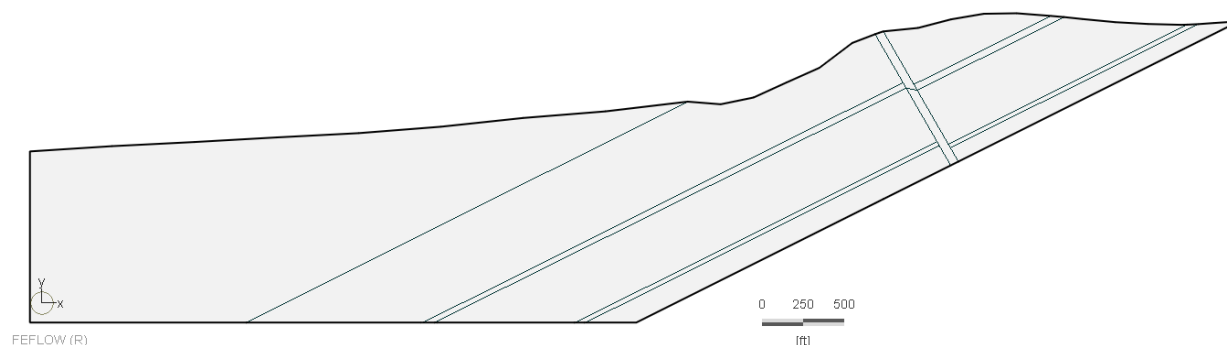
Surface Profile

The surface profile was created using the path measure tool and the elevation profile viewer in GoogleEarth®. A screenshot of the profile is shown here:



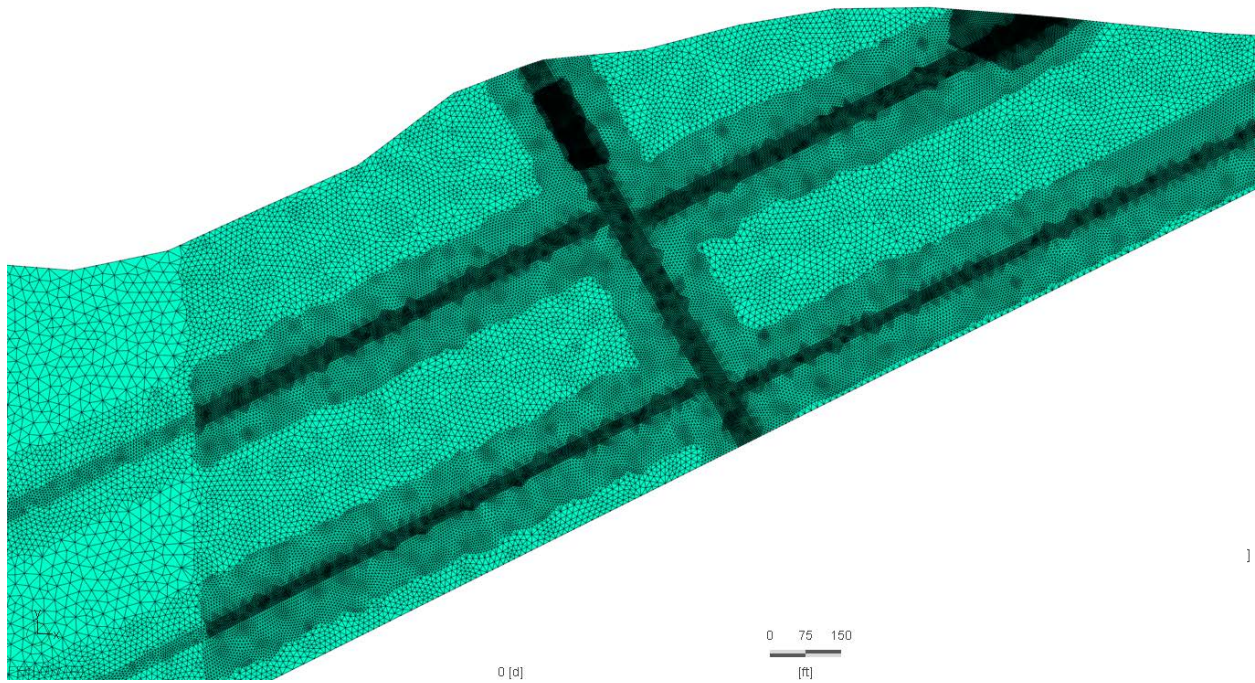
2-D Supermesh

The supermesh was created in FEFLOW® using the drawing tools. The supermesh consisted of 13 polygons corresponding to the hydrostratigraphic units and the upper and lower NFZ. Building the supermesh as separate polygons allows for more flexibility when creating the finite element mesh. The supermesh with the individual polygons is shown here:



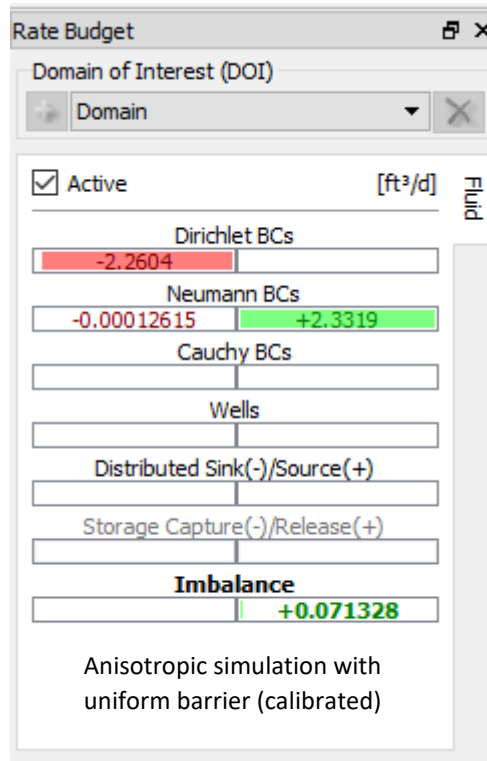
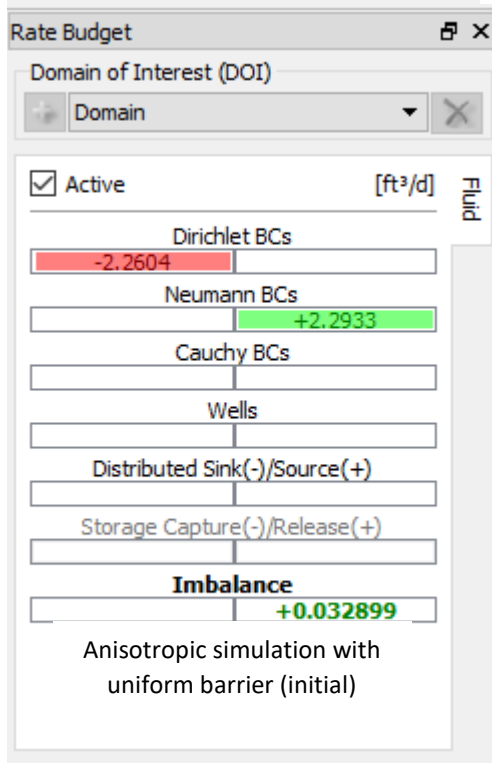
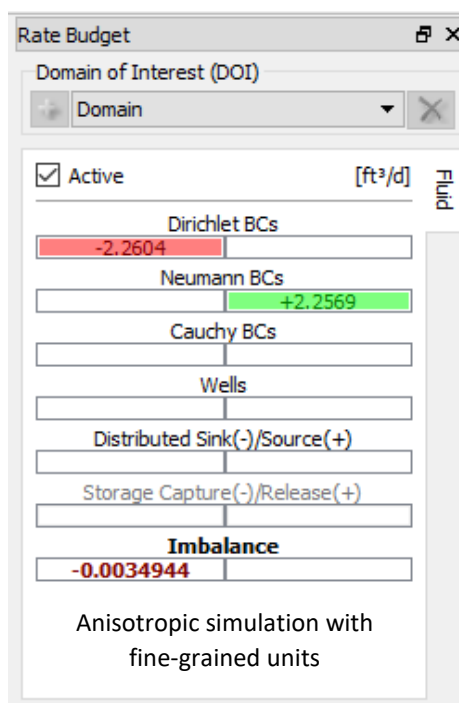
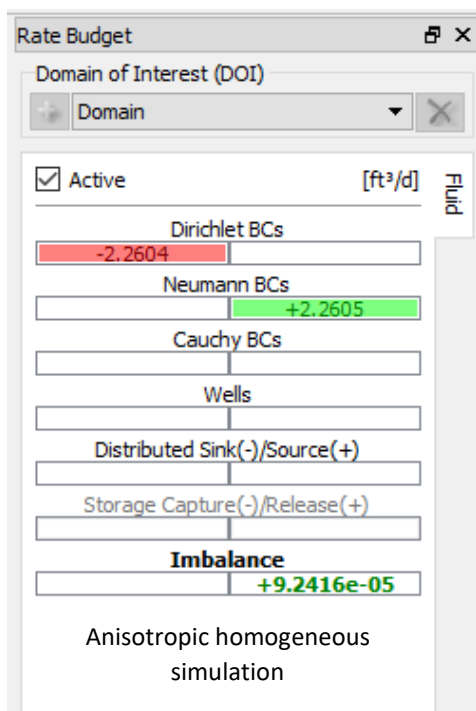
Finite Element Mesh

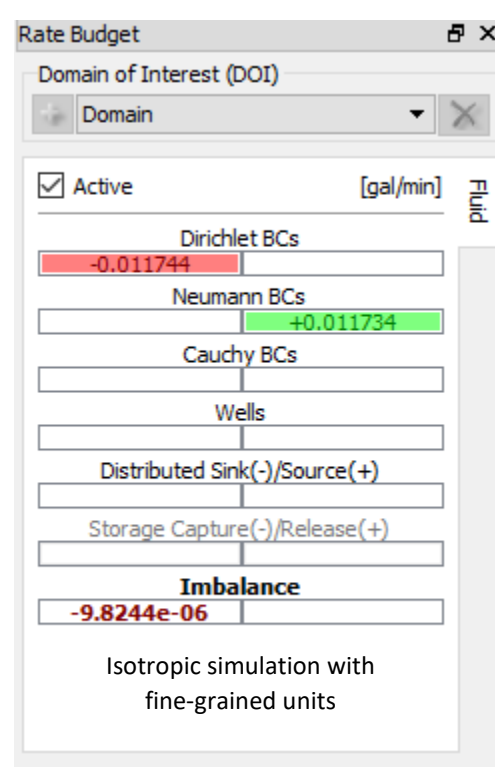
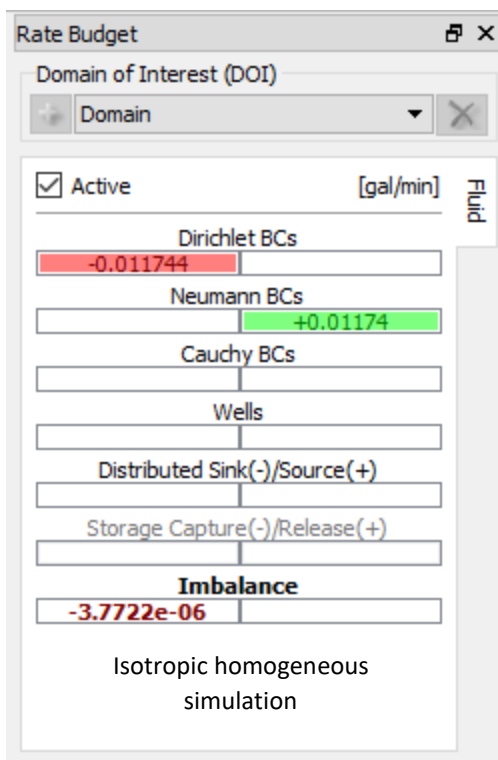
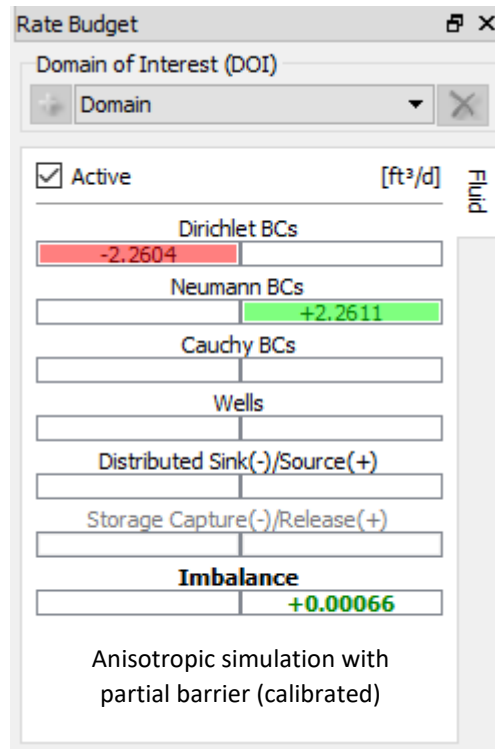
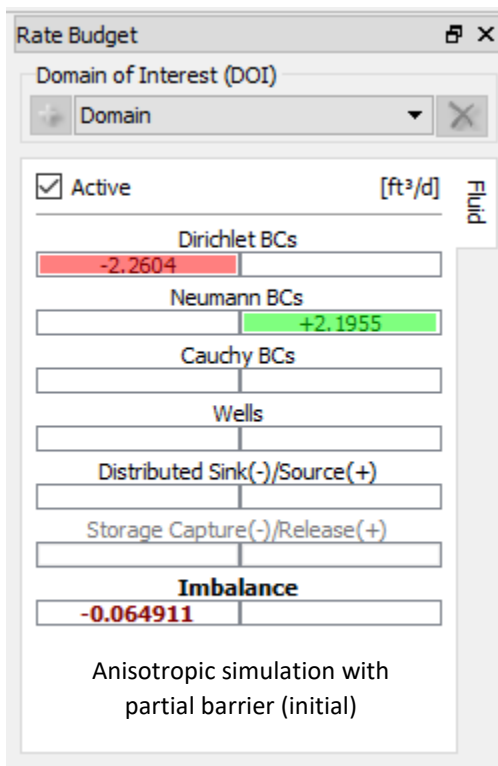
The finite element mesh was created using the Triangle mesh generation algorithm in FEFLOW®. Each polygon was discretized independently. Additional refinement was done as needed to obtain more accurate solutions. Graded refinement was done to have smoother refinement transitions. The ideal element shape is an equilateral triangle. Therefore, mesh smoothing was done to minimize the interior angle of the triangles. The final mesh is shown here:

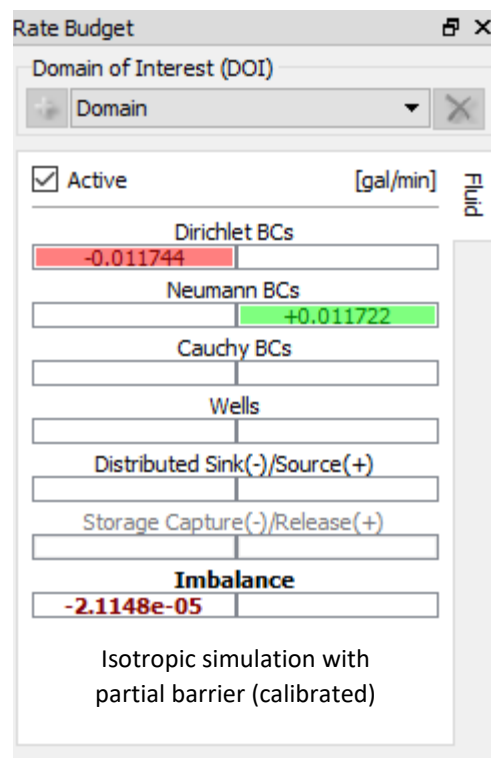
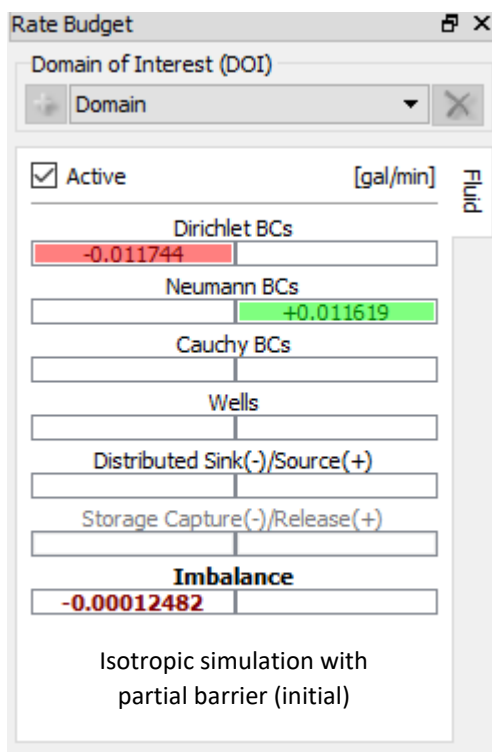
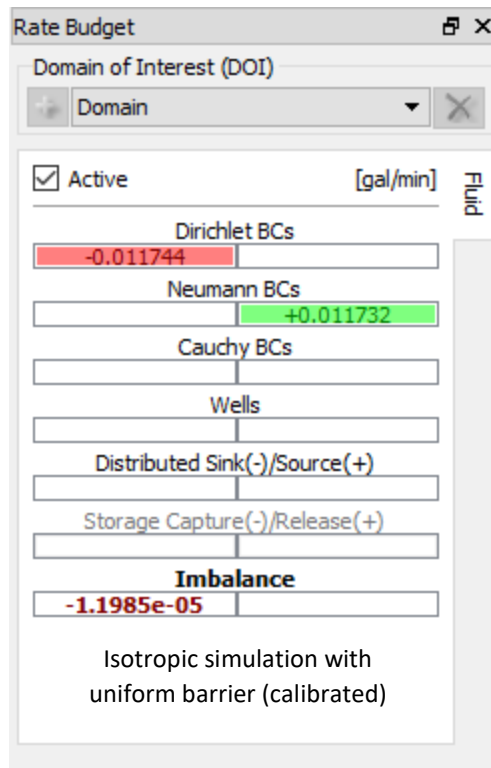
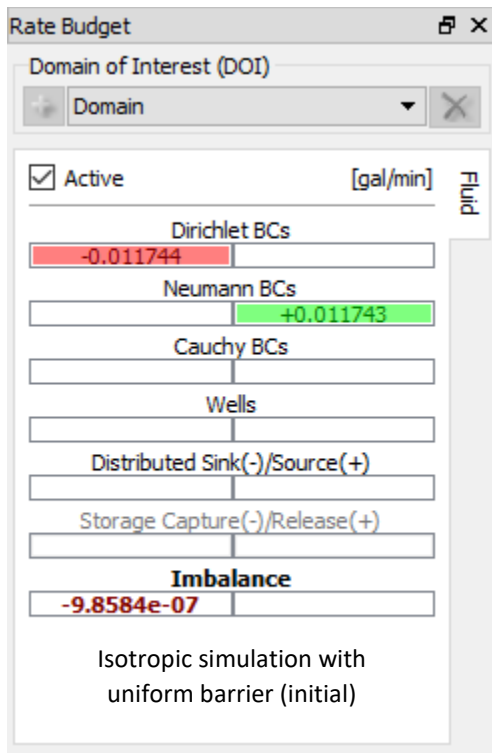


Appendix B: Solution Validation

In a steady-state model, inflow must equal outflow. If there was a significant imbalance between inflow and outflow, it was an indication that something in the model was not working correctly. The rate budget panel in FEFLOW® keeps displays the inflows and outflows and calculates the imbalance. Screen shots of the rate budget for each simulation are shown here:







Appendix C: Water Level Data

The table below shows the well data that was used to import observations points into FEFLOW®. The coordinates of well screens and water levels were provided by CH2M Hill. The Node, Slice and Ref_ParID columns are necessary for importation into FEFLOW.

ID	Dist. from N boundary (X) (ft)	Screen Depth (Y) (ft)	Reference WL (ft)	Reference Residual (ft)	NODE	SLICE	REF_PARID
RD-68A	4008	1215	1325	50	0	1	400
RD-68B	4008	1035	1325	50	0	1	400
ND-124-1	4922	1450	1454.5	100	0	1	400
ND-124-2	4922	1352	1453.5	100	0	1	400
ND-124-3	4922	1276	1452.4	100	0	1	400
ND-124-4	4922	1229	1598	100	0	1	400
RD-56A-2	5108	1385	1389.7	75	0	1	400
RD-56A-3	5108	1360	1374.4	75	0	1	400
RD-56B	5118	1298	1599.8	75	0	1	400
ND-122-1	5382	1654	1678.3	50	0	1	400
ND-122-2	5382	1550	1665.6	50	0	1	400
ND-122-3	5382	1484	1657.2	50	0	1	400
RD-60	5683	1744	1746.1	50	0	1	400
ND-128-1	5808	1699	1729.9	50	0	1	400
ND-128-2	5808	1621	1709.0	50	0	1	400
ND-128-3	5808	1490	1713.8	50	0	1	400
RD-26	6036	1721	1744.6	50	0	1	400
WS-07	6087	1426	1741.7	50	0	1	400